The Astronomical Journal, 168:140 (21pp), 2024 September https://doi.org/10.3847/1538-3881/ad57be

Astrometry and Precise Radial Velocities Yield a Complete Orbital Solution for the Nearby Eccentric Brown Dwarf LHS 1610 b

Evan Fitzmaurice[1,2,3,21], Guðmundur Stefánsson[4,5,22], Robert D. Kavanagh[4,6], Suvrath Mahadevan[1,2], Caleb I. Cañas[7,23], Joshua N. Winn[5], Paul Robertson[8], Joe P. Ninan[9], Simon Albrecht[10], J. R. Callingham[6,11], William D. Cochran[12,13], Megan Delamer[1,2], Eric B. Ford[1,2,3,14], Shubham Kanodia[15], Andrea S. J. Lin[1,2], Marcus L. Marcussen[10], Benjamin J. S. Pope[16,17], Lawrence W. Ramsey[1,2], Arpita Roy[18], Harish Vedantham[6,19], and Jason T. Wright[1,2,20]

[1] Department of Astronomy & Astrophysics, Pennsylvania State University, University Park, PA 16802, USA; exf5296@psu.edu
[2] Center for Exoplanets and Habitable Worlds, Pennsylvania State University, University Park, PA 16802, USA
[3] Institute for Computational and Data Sciences, The Pennsylvania State University, University Park, PA 16802, USA
[4] Anton Pannekoek Institute for Astronomy, University of Amsterdam, 1090 GE Amsterdam, The Netherlands
[5] Department of Astrophysical Sciences, Princeton University, 4 Ivy Lane, Princeton, NJ 08540, USA
[6] ASTRON, Netherlands Institute for Radio Astronomy, Oude Hoogeveensedijk 4, Dwingeloo, 7991 PD, The Netherlands
[7] NASA Goddard Space Flight Center, 8800 Greenbelt Road, Greenbelt, MD 20771, USA
[8] Department of Physics & Astronomy, The University of California, Irvine, Irvine, CA 92697, USA
[9] Department of Astronomy and Astrophysics, Tata Institute of Fundamental Research, Homi Bhabha Road, Colaba, Mumbai 400005, India
[10] Stellar Astrophysics Centre, Department of Physics and Astronomy, Aarhus University, Ny Munkegade 120, 8000 Aarhus C, Denmark
[11] Leiden Observatory, Leiden University, PO Box 9513, 2300 RA, Leiden, The Netherlands
[12] McDonald Observatory and Department of Astronomy, The University of Texas at Austin, 2515 Speedway, Austin, TX 78712, USA
[13] Center for Planetary Systems Habitability, The University of Texas at Austin, 2515 Speedway, Austin, TX 78712, USA
[14] Center for Astrostatistics, 525 Davey Laboratory, The Pennsylvania State University, University Park, PA 16802, USA
[15] Earth and Planets Laboratory, Carnegie Institution for Science, 5241 Broad Branch Road, NW, Washington, DC 20015, USA
[16] School of Mathematics & Physics, University of Queensland, St Lucia, QLD 4072, Australia
[17] Centre for Astrophysics, University of Southern Queensland, West Street, Toowoomba, QLD 4350, Australia
[18] Astrophysics & Space Institute, Schmidt Sciences, New York, NY 10011, USA
[19] Kapteyn Astronomical Institute, University of Groningen, Landleven 12, NL-9747AD Groningen, The Netherlands
[20] Penn State Extraterrestrial Intelligence Center, 525 Davey Laboratory, The Pennsylvania State University, University Park, PA 16802, USA
Received 2023 October 11; revised 2024 June 5; accepted 2024 June 5; published 2024 September 2

Abstract

The LHS 1610 system consists of a nearby ($d = 9.7$ pc) M5 dwarf hosting a candidate brown dwarf companion in a 10.6 days, eccentric ($e \sim 0.37$) orbit. We confirm this brown dwarf designation and estimate its mass ($49.5^{+4.3}_{-3.5}$ $M_{\rm Jup}$) and inclination ($114.5^{\circ+7.4}_{-10.0}$) by combining discovery radial velocities (RVs) from the Tillinghast Reflector Echelle Spectrograph and new RVs from the Habitable-zone Planet Finder with the available Gaia astrometric two-body solution. We highlight a discrepancy between the measurement of the eccentricity from the Gaia two-body solution ($e = 0.52 \pm 0.03$) and the RV-only solution ($e = 0.3702 \pm 0.0003$). We discuss possible reasons for this discrepancy, which can be further probed when the Gaia astrometric time series become available as part of Gaia Data Release 4. As a nearby mid-M star hosting a massive short-period companion with a well-characterized orbit, LHS 1610 b is a promising target to look for evidence of sub-Alfvénic interactions and/or auroral emission at optical and radio wavelengths. LHS 1610 has a flare rate (0.28 ± 0.07 flares per day) on the higher end for its rotation period (84 ± 8 days), similar to other mid-M dwarf systems such as Proxima Cen and YZ Ceti that have recent radio detections compatible with star–planet interactions. While available Transiting Exoplanet Survey Satellite photometry is insufficient to determine an orbital phase dependence of the flares, our complete orbital characterization of this system makes it attractive to probe star–companion interactions with additional photometric and radio observations.

Unified Astronomy Thesaurus concepts: Brown dwarfs (185); Low mass stars (2050); Radial velocity (1332); Astrometry (80)

Materials only available in the online version of record: data behind figures

1. Introduction

The Gaia mission (Gaia Collaboration et al. 2016) is revolutionizing the field of astrophysics, yielding insights into planets, brown dwarfs, and binary stars. The expected detection yield of substellar objects from Gaia—including both exoplanets and brown dwarfs—has been estimated to be thousands to tens of thousands (Lattanzi et al. 2000; Sozzetti et al. 2001; Perryman et al. 2014; Holl et al. 2023). Recently, new detections of substellar objects have been enabled through studying proper-motion differences between Hipparcos and Gaia, allowing

[21] Institute for Computational and Data Sciences Scholar.
[22] NASA Sagan Fellow.
[23] NASA Postdoctoral Fellow.

follow-up observations through direct imaging and/or radial velocities (RVs) to gain insights into brown dwarfs (e.g., Brandt et al. 2021; Li et al. 2023) and giant planets (Currie et al. 2023). Previous studies have shown evidence for different formation mechanisms of brown dwarfs and giant planets (Chabrier et al. 2014), e.g., through their different eccentricity distributions (Bowler et al. 2020). Detailed characterization of the orbital parameter distributions of substellar companions—spanning both brown dwarfs and planetary companions—can yield further insights into how these distinct populations of companions form and evolve.

As part of Gaia Data Release 3 (DR3; Gaia Collaboration et al. 2023), 169,277 Gaia two-body solutions were published assuming a single Keplerian model derived from the first 34 months of Gaia observations (Halbwachs et al. 2023). These two-body solutions provide constraints on all orbital elements, including the orbital period, eccentricity, inclination, mass of the companion, and correlation matrices between the parameters assuming a "dark" companion which contributes no light to the photocenter motion measured by Gaia. Most of these solutions are double-star systems, with 1162 that are likely to be substellar objects analyzed with a dedicated "exoplanet" pipeline (Holl et al. 2023). Recent work by Winn (2022) provided an analysis of planet candidates with Gaia two-body solutions, providing a framework to analyze the two-body solutions along with available RV data, which in some cases highlights good agreement with the Gaia solutions, and sometimes inconsistencies. Recent follow-up observations by Marcussen & Albrecht (2023) further highlight the importance of ground-based observations to confirm and/or rule out false-positive scenarios, such as binaries.

Among different stars, nearby M dwarfs are particularly suitable for detecting substellar companions with Gaia, as they maximize the likelihood of high-precision orbit and mass determination (Perryman et al. 2014; Sozzetti et al. 2014). Around M dwarfs, Sozzetti et al. (2014) predicted the detection of ∼100 giant planets at orbits within 3 au within 30 pc, and ∼2000 within 100 pc. Such a large sample can place tight constraints on the occurrence rates of substellar companions around M dwarfs, which still remains poorly constrained. Detecting giant planets around M dwarfs is particularly valuable, as current models do not predict their formation due to the expected inventory of material in the disk being too low (e.g., Miguel et al. 2020; Burn et al. 2021). Such systems of nearby M stars hosting close-in companions are also prime candidates to search for possible signatures of sub-Alfvénic interactions at optical and radio wavelengths to gain insights into the magnetic environments of the orbiting companion (e.g., Callingham et al. 2021; Kavanagh & Vedantham 2023).

In this paper, we perform a detailed characterization of the LHS 1610 system, the second-closest M dwarf with a substellar companion and a Gaia two-body solution. The only closer M-dwarf system with a substellar companion and Gaia two-body solution is the planetary system GJ 876 (Rivera et al. 2005). LHS 1610 b was originally detected by Winters et al. (2018), before Gaia two-body solutions were available. They characterized it as a mid-M dwarf system that hosts a likely brown dwarf in a $P = 10.6$ days eccentric orbit with a minimum mass of $m \sin i = 44.8 \pm 3.2\ M_{\rm Jup}$ obtained with RVs from the Tillinghast Reflector Echelle Spectrograph (TRES) spectrograph. After the release of the Gaia two-body solutions, the system was highlighted in Gaia Collaboration et al. (2023), where the Gaia astrometric fit independently confirms the orbit of the brown dwarf, although a joint RV and Gaia two-body solution analysis was not performed. To characterize the LHS 1610 system in further detail, we performed a joint sampling of the Gaia two-body solution along with RVs, including the RVs from TRES from Winters et al. (2018) and new, precise near-infrared (NIR) RVs from the Habitable-zone Planet Finder (HPF) spectrograph (Mahadevan et al. 2012, 2014) on the 10 m Hobby–Eberly Telescope (HET). The combined set of RVs from TRES and HPF constrain a new minimum mass of $44.38 \pm 0.67\ M_{\rm Jup}$. The joint sampling allows us to make a new estimate of the orbital inclination of the companion, and thereby its mass of $M = 49.5^{+4.3}_{-3.5}\ M_{\rm Jup}$, confirming that the companion is a brown dwarf. Using available Transiting Exoplanet Survey Satellite (TESS) data, we derive a flare rate for LHS 1610 and compare it to other M star flare rates and their rotation periods from Pope et al. (2021) and Medina et al. (2020, 2022). We find that LHS 1610 resides at the high end of flare rates for its long rotation period for mid-M stars, similar to other mid-M stars such as Proxima Centauri, YZ Ceti, and GJ 1151. These stars are promising candidates for sub-Alfvénic interactions due to known companions (Anglada-Escudé et al. 2016; Stock et al. 2020; Faria et al. 2022; Blanco-Pozo et al. 2023) and radio detections (Vedantham et al. 2020; Callingham et al. 2021; Pérez-Torres et al. 2021; Pineda & Villadsen 2023; Trigilio et al. 2023). This leads us to speculate if the flaring of LHS 1610 is influenced by interactions with its companion. Since additional investigation is necessary to confirm or rule out that scenario, we assess the feasibility of making such a detection. Due to the large size of the short-period companion around a nearby low-mass star, we show that the system is particularly favorable for the detection of possible sub-Alfvénic interactions and potential auroral emission from the brown dwarf at radio wavelengths. We provide a framework for future inquiries into star–planet/star–companion interactions using fully characterized orbits via Gaia two-body solutions and ground-based RVs.

This paper is structured as follows. In Section 2, we discuss the parameters of the host star, and we discuss the observations analyzed in Section 3. In Section 4, we discuss our modeling of the Gaia two-body solution and the available RVs, and discuss the accompanying results in Section 5. We place the system in context with other brown dwarf systems in Section 6. In Section 7, we discuss our flare analysis of available TESS data, and energetics of possible sub-Alfvénic interactions or auroral emission in the system. We conclude with a summary of our findings in Section 8.

2. Stellar Parameters

To characterize the spectroscopically determined $T_{\rm eff}$, [Fe/H], and $\log g$ parameters, we used the `HPF-SpecMatch` (Stefansson et al. 2020) code, which compares an as-observed spectrum with HPF to a library of well-characterized spectra. In doing so, we realized that LHS 1610 is listed in the input library from Yee et al. (2017), with an effective temperature $T_{\rm eff} = 3079 \pm 60$ K, metallicity $[{\rm Fe/H}] = 0.01 \pm 0.08$, and $\log g = 5.04 \pm 0.06$, as originally determined in Mann et al. (2015). As a test, we removed the LHS 1610 spectrum from the library, and we ran it through the `HPF-SpecMatch` algorithm, recovering consistent values. We elected to adopt the spectroscopically determined measurements as originally reported in Mann et al. (2015). Additionally, the `HPF-SpecMatch` analysis further confirms a low projected rotational velocity of $v \sin i < 2$ km s^{-1}, agreeing with the

Table 1
Summary of Stellar Parameters Used in This Work

Parameter	Description	Value	Reference
SpT	Spectral type	M5	(1)
$T_{\rm eff}$	Effective temperature	3079 ± 60 K	(2)
[Fe/H]	Metallicity	0.01 ± 0.08	(2)
$\log(g)$	Surface gravity (cgs)	5.04 ± 0.06	(2)
R_*	Radius	$0.2007^{+0.0071}_{-0.0063} R_\odot$	This work
Age	Age	$7.0^{+4.5}_{-4.7}$ Gyr	This work
M_*	Mass	$0.1671 \pm 0.0041\ M_\odot$	This work
RV	Systemic RV	43.1 ± 0.1 km s^{-1}	This work
d	Distance	$9.6625^{+0.0090}_{-0.0088}$ pc	(3)
ϖ	Parallax	$103.879^{+0.023}_{-0.023}$ mas	(4)
$P_{\rm rot}$	Rotation period	84.3 ± 8 days	(1)
$v \sin i$	Rotational velocity	<2 km s^{-1}	This work
$R_{\rm flare}$	Flare rate[a]	0.28 ± 0.07 day^{-1}	This work
$\ln R_{31.5}$	"High-energy" flare rate[b]	-2.51 ± 0.45 day^{-1}	This work

Notes.
References: (1) Winters et al. (2018), (2) Mann et al. (2015), (3) Bailer-Jones et al. (2018), (4) Gaia. Winters et al. (2018) report a rotation period of 84.3 days with a 5%–10% error. We adopt a 10% rotation period error.
[a] Derived following the methodology in Pope et al. (2021).
[b] Derived following the methodology in Medina et al. (2020, 2022).

long rotation period from Winters et al. (2018) of $P = 84.3$ days, which was securely measured using long-term ground-based photometric monitoring from MEarth (Nutzman & Charbonneau 2008; Irwin et al. 2015).

To obtain constraints on the mass, radius, and age of the system, we performed a fit to the spectral energy distribution (SED) of LHS 1610 using available literature magnitudes of the star using the `EXOFASTv2` (Eastman et al. 2019) code and MESA Isochrones and Stellar Tracks (MIST; Choi et al. 2016; Dotter 2016) isochrones. As an input for the SED fit, we used informative priors on the spectroscopically determined $T_{\rm eff}$, [Fe/H], and $\log g$ parameters as listed above. In doing so, we obtain a mass of $M = 0.167^{+0.014}_{-0.015}\ M_\odot$ and a radius of $R = 0.2007^{+0.0071}_{-0.0063}\ R_\odot$. As a separate constraint on the stellar mass, we used the M–K relation from Mann et al. (2019), where we find a stellar mass of $M = 0.1671 \pm 0.0041\ M_\odot$. This agrees with the stellar mass from the SED fit, but is more precise. We elected to adopt the mass from the M–K relation, as the relation has been tightly calibrated for mid-to-late M dwarfs. Table 1 summarizes our adopted stellar parameters.

3. Observations

3.1. Tillinghast Reflector Echelle Spectrograph Optical Radial Velocities

We use RVs of LHS 1610 from Winters et al. (2018), which used the TRES. There are a total of 13 RVs, which have a median RV uncertainty of 28.3 m s^{-1} and span 39 days. The spectra were taken with 900 s exposures in good conditions, and longer in poor conditions. The medium fiber was used with a resolving power of $R \sim 44{,}000$. The signal-to-noise ratio (S/N) was 15 per pixel at 7150 Å. The RVs were extracted using the pipeline described in Buchhave et al. (2010), and are shown in Panel A of Figure 1.

3.2. Habitable-zone Planet Finder Near-infrared Radial Velocities

We acquired precise RVs from the spectra of LHS 1610 using the HPF spectrograph (Mahadevan et al. 2012, 2014). HPF is a fiber-fed NIR spectrograph on the 10 m HET (Ramsey et al. 1998; Shetrone et al. 2007; Hill et al. 2021) at McDonald Observatory in Texas, covering the z, Y, and J bands from 810 to 1280 nm at a resolving power of $R \sim 55{,}000$. To enable precise RVs in the NIR, the HPF is temperature-stabilized at the millikelvin level (Stefansson et al. 2016). We extracted the HPF RVs using a modified version of the SpEctrum Radial Velocity AnaLyzer (`SERVAL`; Zechmeister et al. 2018), adapted for HPF following Metcalf et al. (2019), Stefansson et al. (2020), and Stefánsson et al. (2023).

In total, we obtained six HPF observations, which have a median S/N of 158 at 1 μm and a median RV uncertainty of 4.7 m s^{-1}. The RVs span 528 days, significantly expanding the total observational baseline. Three of the RV points are the average of two 969 s exposures taken in the same night. Two of the RV points are singular 969 s exposures, and the final RV point comes from a spectrum taken with an exposure time of 191 s. The RVs are shown in Panel B of Figure 1, and listed in Table 4.

3.3. Gaia Two-body Solution

As part of Gaia DR3, fits indicating two bodies are reported in the Gaia Archive (under `nss_two_body_orbits`). These two-body fits contain best-fit results for parameters along with a correlation matrix quantifying the correlation between the parameters. We convert the correlation matrix to a covariance matrix using `nsstools` (Halbwachs et al. 2023).[24] There were 445 astrometric CCD observations used for the Gaia two-body solution fit of LHS 1610 as provided by the Gaia team. Relevant Campbell elements from the Gaia two-body solution are listed in column (4) of Table 2.

3.4. Transiting Exoplanet Survey Satellite Photometry

LHS 1610 was observed by TESS (Ricker 2015) in Sectors 42 (2021 August 20–2021 September 16), 43 (2021 September 16–2021 October 12), and 44 (2021 October 12–2021 November 6). In the TESS Input Catalog (TIC; Stassun et al. 2018, 2019), LHS 1610 is listed as TIC 242941982. LHS 1610 shows flares in each TESS sector; the TESS sectors with highlighted flares are shown in Appendix A. We determine the flare rate, and put this rate in context with other M dwarfs in Section 7.1.

4. Modeling of Astrometry and Radial Velocities

To characterize the system, we compare the results from three different methods: (1) the Gaia two-body solution, (2) a fit of the RVs ("RV-only fit"), and (3) a joint sampling of both the Gaia two-body solution and the available RVs. For the joint sampling, we broadly follow the methodology outlined in Winn (2022). The three models and values are further described below.

[24] https://www.cosmos.esa.int/web/gaia/dr3-nss-tools

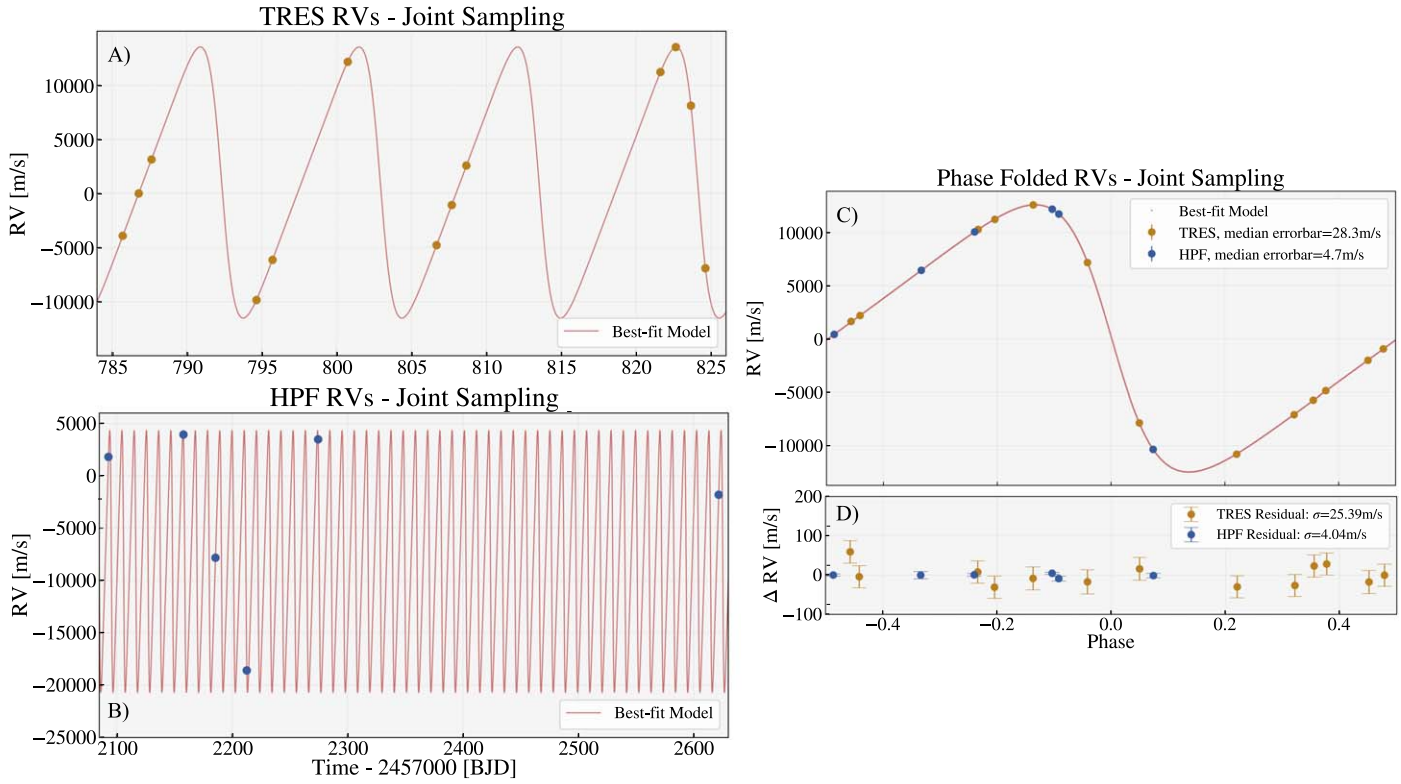

Figure 1. Visualization of joint Gaia-RV sampling with inflation. A: RVs using TRES from Winters et al. (2018), with our best-fit model laid over the points. B: our new RVs using HPF, with the best-fit model in red. This shows the significant increase in the observing baseline provided by the additional HPF RVs, which span more than 500 days. C and D: phase-folded RVs and residuals using the parameters produced by the joint sampling. Both sets of RVs are in agreement with the best-fit model. Errors in panels A, B, and C are smaller than the marker size. The RVs are available as the data behind the figure.
(The data used to create this figure are available in the online article.)

Table 2
Results from the Methods Considered in This Work

Parameter	RV-only Fit	Gaia Two-body Solution	Gaia+RV $\sigma_{\rm scale} \equiv 1$[a]	Gaia+RV $\sigma_{\rm scale} > 1$ (adopted)
M_* ($M_\odot$)	…	…	$0.1672^{+0.0041}_{-0.0041}$	$0.1672^{+0.0041}_{-0.0041}$
m_2 ($M_{\rm Jup}$)	…	…	$50.94^{+0.89}_{-0.90}$	$49.5^{+4.3}_{-3.5}$
$\cos i$	…	…	$-0.457^{+0.014}_{-0.014}$	$-0.41^{+0.17}_{-0.17}$
i (deg)	…	$92.8^{+1.9}_{-1.9}$	$117.19^{+0.88}_{-0.91}$	$114.5^{+7.4}_{-10.0}$
K (m s^{-1})	$12534.6^{+9.7}_{-9.6}$	…	$12540.7^{+9.7}_{-9.7}$	$12534.7^{+9.8}_{-9.6}$
e	$0.37019^{+0.00030}_{-0.00030}$	$0.524^{+0.027}_{-0.027}$	$0.37004^{+0.00030}_{-0.00030}$	$0.37018^{+0.00030}_{-0.00030}$
ω (deg)	$89.22^{+0.14}_{-0.14}$	$271.4^{+2.9}_{-2.9}$	$89.31^{+0.14}_{-0.14}$	$89.22^{+0.14}_{-0.14}$
Ω (deg)	…	$162.6^{+1.5}_{-1.5}$	$-14.9^{+0.82}_{-0.81}$	$-14.6^{+8.3}_{-7.7}$
$t_{\rm peri}$ (days)[b]	$0.7107^{+0.0031}_{-0.0031}$	$0.61^{+0.15}_{-0.15}$	$0.7119^{+0.0031}_{-0.0031}$	$0.7107^{+0.0032}_{-0.0031}$
P (days)	$10.594724^{+0.000016}_{-0.000016}$	$10.5885^{+0.0013}_{-0.0013}$	$10.594733^{+0.000016}_{-0.000016}$	$10.59472^{+0.000020}_{-0.000016}$
ϖ (mas)	…	…	$103.881^{+0.023}_{-0.023}$	$103.879^{+0.023}_{-0.023}$
$\gamma_{\rm TRES}$ (m s^{-1})	$945.2^{+8.2}_{-8.2}$	…	$944.0^{+8.2}_{-8.2}$	$945.2^{+8.2}_{-8.2}$
$\gamma_{\rm HPF}$ (m s^{-1})	$8244.1^{+3.2}_{-3.2}$	…	$-8245.7^{+3.2}_{-3.2}$	$-8244.1^{+3.2}_{-3.2}$
$\sigma_{\rm scale}$	…	…	$\equiv 1$	$9.0^{+4.2}_{-2.5}$
a_0 (mas)	…	$1.391^{+0.037}_{-0.037}$	$1.325^{+0.011}_{-0.011}$	$1.294^{+0.093}_{-0.078}$
A (mas)	…	$-0.053^{+0.067}_{-0.067}$	$-0.140^{+0.009}_{-0.010}$	$-0.108^{+0.086}_{-0.089}$
B (mas)	…	$-0.055^{+0.051}_{-0.051}$	$-0.589^{+0.023}_{-0.023}$	$-0.52^{+0.23}_{-0.19}$
F (mas)	…	$-1.327^{+0.037}_{-0.037}$	$-1.282^{+0.012}_{-0.012}$	$-1.246^{+0.085}_{-0.098}$
G (mas)	…	$0.418^{+0.035}_{-0.035}$	$0.334^{+0.018}_{-0.018}$	$0.32^{+0.16}_{-0.19}$

Notes. In the Gaia+RV jointly sampled constraints we fix the flux ratio parameter at $\varepsilon = 0$. The $\sigma_{\rm scale} = 1$ sampling shows evidence of inconsistencies and likely has underestimated uncertainties. To better account for these inconsistencies, we adopt the jointly sampled Gaia+RV values, where we let the $\sigma_{\rm scale}$ parameter float, which results in more conservative uncertainties. We note that these values need to be revisited when the Gaia Data Release 4 astrometric time series become available.
[a] Uncertainties are likely underestimated. See Section 5.3.1 for further discussion.
[b] For the periastron time, we follow the Gaia convention where the periastron time is $t_{\rm peri} = 2457389.0 + t_p$, where t_p is the value listed in the table above.

4.1. Gaia Two-body Solution

The two-body solution from the Gaia DR3 `nss_two_body_orbits` table yields constraints on the following parameters:

$$A, B, F, G, e, P, t_p, \varpi, \tag{1}$$

where e is the eccentricity, P is the period, ϖ is the parallax, and t_p is the periastron time referenced to epoch 2016.0 (JD 2,457,389.0). A, B, F, and G are the Thiele–Innes coefficients:

$$A = a_0(\cos\omega\,\cos\Omega - \sin\omega\,\sin\Omega\,\cos i), \tag{2}$$

$$B = a_0(\cos\omega\,\sin\Omega + \sin\omega\,\cos\Omega\,\cos i), \tag{3}$$

$$F = -a_0(\sin\omega\,\cos\Omega + \cos\omega\,\sin\Omega\,\cos i), \tag{4}$$

$$G = -a_0(\sin\omega\,\sin\Omega - \cos\omega\,\cos\Omega\,\cos i), \tag{5}$$

where a_0 is the semimajor axis of the photocenter converted to milliarcseconds by multiplying by the parallax, ω is the argument of periastron, Ω is the longitude of the ascending node, and i is the inclination. We use the covariance matrix and `nsstools` to use the Thiele–Innes coefficients to yield constraints on ω, Ω, i, and a_0. Halbwachs et al. (2023) discuss the ranges of these elements and their physical interpretation from the Gaia two-body solution fits. The astrometric fit uniquely constrains the orbital inclination to the physical motion of the orbit, where orbital inclinations between $[0, \frac{\pi}{2}]$ indicate a counterclockwise orbit, while values between $[\frac{\pi}{2}, \pi]$ indicate a clockwise orbit. Due to a degeneracy of π in Ω and ω, the Gaia astrometric orbit fits will have two equivalent possible solutions and, as noted by Halbwachs et al. (2023), the solution provided in the Gaia two-body solution table is the solution where Ω is between $[0, \pi]$ and ω is between $[0, 2\pi]$.

4.2. RV-only Fit

For the RV-only fit, we use the following as parameters in the fit:

$$P, t_p, e, \omega, K, \gamma, \tag{6}$$

where K is the RV semi-amplitude, and γ is the RV offset for the spectrograph combined with the stellar RV offset. We fit a new γ for each individual spectrograph. We compute the Keplerian RV model using the `radvel` code (Fulton et al. 2018). RVs alone allow us to uniquely constrain the value of ω but not the inclination, meaning we cannot determine the true mass of the secondary, only its minimum mass.

The Doppler likelihood function is

$$\mathcal{L}_v = \prod_{i=1}^{N} \frac{1}{\sqrt{2\pi(\sigma_{v,i}^2)}} \exp\left[-\frac{(v_i - v_{i,\mathrm{calc}})^2}{2(\sigma_{v,i}^2)}\right], \tag{7}$$

where v_i is the ith RV data point, $\sigma_{v,i}$ is the associated uncertainty, and $v_{i,\mathrm{calc}}$ is the ith model calculated RV. In practice, we take the log of Equation (7) so that we can sum the log value of every ith step.

To fit the RVs, we use the differential evolution package `PyDE` (Parviainen 2016) to determine a global maximum-likelihood solution of a Keplerian RV model to the RV observations. We then initialize 100 Markov Chain Monte Carlo (MCMC) walkers around the global maximum-likelihood solution to perform MCMC sampling of the parameter posteriors using the `emcee` package (Foreman-Mackey et al. 2013). We ran the walkers for 35,000 steps. After removing a burn-in of 2000 chains, we assess the convergence of the chains with two metrics. First, we compute the Gelman–Rubin statistic and confirm its value for each parameter is within 1% of unity. This statistic can be unreliable if the chains are not independent (see, e.g., discussion in Hogg & Foreman-Mackey 2018). Therefore, we additionally computed the maximum autocorrelation timescale and adjust the number of chains in the MCMC to be longer than 50 times this value to ensure a sufficient number of independent samples.[25] We find the mean autocorrelation time to be 78 and the maximum to be 109, so from these steps, along with visual inspections of the chains, we conclude that the chains are well mixed.

4.3. Joint Astrometry and RV Sampling

To jointly sample the Gaia astrometric covariance matrix and the available RVs, we use the following parameters:

$$M_*,\ m_2,\ e,\ \omega,\ \cos i,\ \Omega,\ P,\ t_p,\ \varpi,\ \gamma,\ \varepsilon,\ \sigma_{\mathrm{scale}}, \tag{8}$$

where M_* is the stellar mass, m_2 is the secondary mass, $\cos i$ is the cosine of the inclination, ε is the flux ratio between the companion and star, and σ_{scale} is a scaling factor that acts as a jitter term for the two-body solution and is discussed below. All of the Gaia parameters are relative to the photocenter since Gaia measures the center of light between the star and any potentially unresolved companions. ε is involved when computing the a_0 for a given set of parameters:

$$\frac{a_0}{\varpi} = [G(M_* + m_2)]^{\frac{1}{3}}\left(\frac{P}{2\pi}\right)^{\frac{2}{3}}\left(\frac{m_2}{M_* + m_2} - \frac{\varepsilon}{1+\varepsilon}\right). \tag{9}$$

Like the RV-only fit, we fit individual RV offsets for HPF and TRES.

To sample the Gaia covariance matrix, we modify the Gaia likelihood function from Winn (2022):

$$\mathcal{L}_g = \frac{1}{\sqrt{(2\pi)^8|\det \mathcal{C}_{\mathrm{scale}}|}} \exp\left[-\frac{1}{2}(\Theta^{\mathrm{T}}\mathcal{C}_{\mathrm{scale}}^{-1}\Theta)\right], \tag{10}$$

where $\mathcal{C}_{\mathrm{scale}}$ is the covariance matrix including a multiplicative factor, σ_{scale}, used to optionally scale the full covariance matrix, where

$$\mathcal{C}_{\mathrm{scale}} = \sigma_{\mathrm{scale}}^2 \times \mathcal{C}, \tag{11}$$

where $\mathcal{C}$ is the original covariance matrix from the Gaia two-body solution. σ_{scale} is squared in the above equation to interpret the scaling factor as a multiplicative uncertainty scaling factor rather than a multiplicative variance factor. As σ_{scale} uniformly scales the full covariance matrix, this has the effect of increasing the uncertainties between the different parameters, while keeping the relative correlations between the parameters the same.

Θ is the "Gaia deviation vector," which is an eight-column vector of the differences between the Gaia-reported value and the calculated value for the following parameters:

$$A, B, F, G, e, P, t_p, \varpi. \tag{12}$$

[25] https://emcee.readthedocs.io/en/latest/tutorials/autocorr/

When computing the RV model to determine the RV likelihood in the joint sampling, we calculate the semi-amplitude according to Equation (15) from Winn (2022):

$$K = \frac{2\pi}{P}\frac{(a_0/\varpi)\sqrt{1-\cos^2 i}}{\sqrt{1-e^2}}, \quad (13)$$

while a_0 is calculated using Equation (9).

The total likelihood for the joint sampling is therefore given by

$$\log(\mathcal{L}_{\rm Total}) = \log(\mathcal{L}_g) + \log(\mathcal{L}_v). \quad (14)$$

Similar to the RV-only analysis, we use `PyDE` to find a global maximum-likelihood solution, after which we use `emcee` to perform MCMC sampling of the posteriors. For the analysis, we ran two runs, a joint sampling where $\sigma_{\rm scale}$ is fixed to 1, i.e., using the covariance matrix as is, and another run where $\sigma_{\rm scale}$ is allowed to float, where the latter was done to help account for unexplained discrepancies seen between the RV and the Gaia two-body solution.

For the former sampling where $\sigma_{\rm scale} = 1$, we initialize 100 walkers and run those walkers for 45,000 steps. We removed the first 2500 chains as burn-in chains. Our Gelman–Rubin statistics are all within 1% of unity. The mean autocorrelation timescale is 178, while the maximum is 282, meaning our chains are well mixed.

For the second sampling run where $\sigma_{\rm scale}$ is allowed to float, we initialize 100 walkers and run the walkers for 3,250,000 steps. We removed the first 100,000 steps as burn-in. The Gelman–Rubin statistics are again within 1% of unity for all parameters. The maximum autocorrelation length is 56,730 for the parameters, which is less than 50 times the length of the chains minus the burn-in, suggesting that our chains are well mixed. As mentioned in Sections 4.1 and 4.2, the RVs uniquely constrain ω but not the inclination nor Ω, while the astrometry uniquely constrains inclination but has the π degeneracy for ω and Ω. By jointly sampling the RVs and the astrometric solution, we can constrain all three values and break the degeneracies.

5. Results

Below, we discuss the results from the three different methodologies we used to constrain the orbital parameters of LHS 1610 b: from the available RVs (RV-only), the Gaia two-body solution (Gaia only), and a joint sampling of both the RVs and the Gaia two-body solution with and without a $\sigma_{\rm scale}$ factor for the Gaia covariance matrix. Table 2 summarizes the resulting posteriors from the different methodologies. The results from our final adopted joint-sampling model are graphically summarized in Figure 1.

5.1. RV-only

First, we compare our results in Table 2 from the RV-only fit to the values in Winters et al. (2018). The values we obtain are consistent with the values reported in Winters et al. (2018) which used only RVs from the TRES spectrograph. The additional HPF RVs allow us to significantly improve the precision on multiple parameters, including decreasing the orbital period uncertainty by a factor of 140, and the eccentricity is more tightly constrained as $e = 0.37019 \pm 0.0003$ compared to $e = 0.36942 \pm 0.00093$ from Winters et al. (2018). We experimented running fits with individual RV jitter parameters for TRES and HPF that had Jeffreys priors from 0.1 to 100 m s^{-1}. This returned Keplerian parameter constraints consistent with the fits with no jitter. The jitter estimates were $1.6^{+9.3}_{-1.3}$ m s^{-1} and $4.4^{+8.7}_{-3.9}$ m s^{-1} for TRES and HPF, respectively. The modes of the distributions of the jitter values are 0 m s^{-1}. From this, we interpret that the RV uncertainties provide an accurate estimate of the total uncertainties and we elect to list the posterior results from the RV-only fit without the jitter values. The RVs from TRES and HPF yield a minimum mass constraint of $m_2 \sin(i) = 44.38 \pm 0.67\ M_{\rm Jup}$.

5.2. RV-only versus Gaia Two-body Solution

Second, we compare our RV-only results to the results from the Gaia two-body solution (third column in Table 2). We see that the time of periastron is consistent and the orbital period constraint is broadly in agreement, although with the RV-determined period being much more precise ($P = 10.5885 \pm 0.0013$ day from the Gaia two-body solution, compared to $P = 10.594724 \pm 0.000016$ from the RVs). Additionally, we see that the value for ω between the RV-only and the Gaia two-body solution differ by ~180°. This is a result of the π degeneracy in ω in the astrometric two-body solution fits (see Section 4.1 and Appendix B of Halbwachs et al. 2023). An important note is that the inclination for Gaia sets the direction of the orbit. Since the inclination is between $[\frac{\pi}{2}, \pi]$, the system orbits in a clockwise direction as observed from Earth.

Importantly, Table 2 highlights a discrepancy between the eccentricity of the two solutions, where the Gaia solution suggests an eccentricity of $e = 0.524 \pm 0.027$, while the RV fit suggests an eccentricity of $e = 0.37019 \pm 0.00003$. From the quality of the RVs, the RV-derived eccentricity is reliable, suggesting possible issues with the Gaia two-body solution.

A few possibilities could explain this discrepancy. First, a third body may be present in the system that could be biasing the astrometry. However, we deem this unlikely as the RV residuals do not exhibit additional structure or trends from the single-companion Keplerian fits.

Another possibility could be that the secondary companion is contributing secondary light, breaking the assumption of a dark companion in the Gaia two-body solution. To check if this assumption is warranted in the LHS 1610 system, we estimated the flux ratio, ε, between the brown dwarf and host star in the Gaia bandpass. Using the Sonora–Bobcat spectral templates (Marley et al. 2021) for the brown dwarf, PHOENIX stellar spectral templates (Husser et al. 2013) for the star, and accounting for the transmission curve across the Gaia bandpass, we estimate the flux ratio in the Gaia bandpass (320–1100 nm) to be negligible ($<10^{-6}$). As such, we do not expect light emitted from the brown dwarf to impact the Gaia solution.

The Gaia two-body solution and the associated covariance matrix may not be accurately depicting the shapes of the posteriors of the orbital parameters, but highly structured and/or other nonlinear covariances between different parameters would likely not be accurately estimated using the sampling methodology we used (see further discussion in Winn 2022 and Marcussen & Albrecht 2023).

Additionally, we note that astrometric photocenter motion dominated by motion along one axis in the sky plane can result in biases of the orbital fit, including a bias toward close to edge-on inclinations, which in turn would impact the derived eccentricity. Based on the orbital parameters, the orientation of LHS 1610 b's orbit on the sky suggests motion primarily along the decl. axis. This could help explain the eccentricity

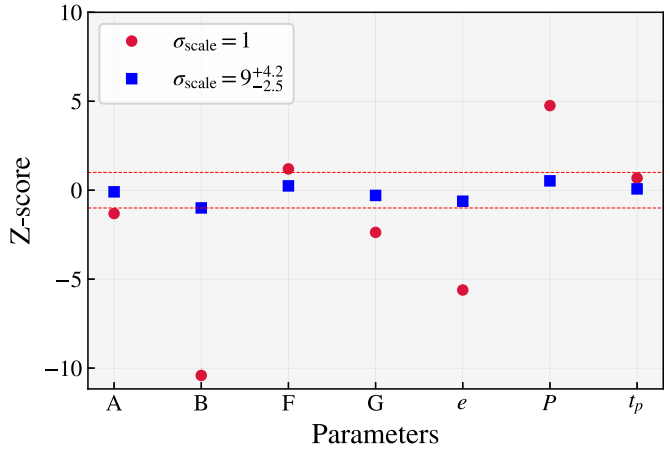

Figure 2. Comparison of Z-score values for the two joint-sampling methodologies we considered. The joint-sampling Z-scores where we fix $\sigma_{\rm scale} = 1$ are shown with red circles. Same as before but where we let $\sigma_{\rm scale}$ be a fit parameter in the MCMC sampling, shown with blue squares. The red dashed lines show Z-score values of ± 1. The former sampling highlights inconsistencies (absolute Z-score values larger than 1) for the parameters e, P, and B. From the latter sampling, we see that through letting $\sigma_{\rm scale}$ inflate the Gaia covariance matrix, this correspondingly increases the uncertainties in the derived parameters (see Table 2) and thus results in Z-scores that are in better agreement (absolute Z-scores <1).

discrepancy given the nearly edge-on inclination of the Gaia two-body solution.

Lastly, the nominal scanning law that dictates how Gaia observes the sky and the resulting projection of the orbit on the detector may also be at play. For more detail, see Holl et al. (2023), which discusses how the along-scan and across-scan angles of Gaia can impact the derived orbital parameters.

5.3. Joint RV+Gaia Sampling

Given the availability of a Gaia two-body solution for LHS 1610 b, we performed a joint sampling of both the Gaia covariance matrix and the RVs. Due to the discrepancies between the RV-only solution and the Gaia two-body solution, we consider two separate joint-sampling models. First, a joint sampling where $\sigma_{\rm scale} = 1$, and second, a joint sampling where we let $\sigma_{\rm scale}$ be a fit parameter.

5.3.1. Joint Sampling with $\sigma_{scale} = 1$

First, we performed a joint sampling of the two-component likelihood function in Equation (14), which includes a likelihood of the Gaia covariance matrix with $\sigma_{\rm scale} = 1$ along with the RV likelihood. The results from this joint sampling are summarized in column (4) of Table 2. From this joint sampling, we find that the orbital period and the eccentricity converges on the RV-derived values with the eccentricity estimated as $e = 0.37004 \pm 0.000030$.

As noted previously, the Gaia astrometric fits have two degenerate solutions for ω and Ω, and the Gaia two-body solution is the solution where Ω is bound to $[0,\pi]$ and ω to $[0,2\pi]$. The RVs break the π degeneracy and informs us of the correct solution, where $\Omega = -14.9^\circ \pm 0.82^\circ$ and $\omega = 89.31^\circ \pm 0.14^\circ$.

This joint sampling results in an inclination of $i = 117.19^{\circ\,+0.88}_{-0.91}$ and a corresponding secondary mass of $50.94 \pm 0.9\ M_{\rm Jup}$. This inclination is 24° greater than the value expected by the Gaia two-body solution of $i = 92.8^\circ \pm 1.9^\circ$. This discrepancy highlights that the uncertainties from this joint sampling are underestimated.

To further assess the quality of the joint sampling, we follow Winn (2022) and we consider the Z-scores of the jointly constrained parameters A, B, F, G, e, P, and $t_{\rm p}$, where the Z-score for a given parameter is calculated as

$$\text{Z}-\text{score} = \frac{x_1 - x_2}{\sigma_{x_2}}, \tag{15}$$

where x_1 and x_2 are two different measurements of the same parameter, and σ_{x_2} is the uncertainty on the x_2 measurement. Here, we define the Z-scores such that x_1 is the median joint-sampling posterior value, x_2 is the median Gaia-only posterior value, and σ_{x_2} is the average of the upper and lower uncertainties on the Gaia-only posterior value. In the case where $\sigma_{\rm scale}$ is a fit parameter, the original Gaia-only uncertainties are multiplied by the median fit value of $\sigma_{\rm scale}$ before computing σ_{x_2}.

Figure 2 shows the Z-scores for the Thiele–Innes coefficients A, B, F, G, along with e, P, and $t_{\rm p}$. From Figure 2, we see that the Z-scores highlight inconsistencies, in particular between the eccentricity e, orbital period P, and the B coefficient. From these inconsistencies, we caution against interpreting these values as the final orbital parameters for LHS 1610 b.

5.3.2. Joint Sampling with σ_{scale} as a Free Parameter

To account for the discrepancies between the Gaia two-body solution and the RV fit, we performed a second sampling of the joint likelihood function where we let $\sigma_{\rm scale}$ be a free parameter in the MCMC sampling. This scales the uncertainties in all of the parameters in the Gaia covariance matrix, while keeping the relative covariances.

The results of this are shown in the fifth column of Table 2 and are graphically summarized in Figure 1. In panels C and D, we see that both the optical TRES and the NIR HPF RVs fully agree on the RV orbit, showing RV residuals with no visually apparent residual structure, suggesting a good fit. We also see that the resulting parameters that are directly constrained by the RVs all fully agree with the RV-only fit in Table 2.

From Table 2, we see that $\sigma_{\rm scale} = 9.0^{+4.2}_{-2.5}$, suggesting that a significant scaling of the Gaia covariance matrix is needed to self-consistently jointly sample the Gaia covarience matrix and the available RVs. As expected, this value of $\sigma_{\rm scale}$ results in larger uncertainties in the astrometric parameters, including the inclination of $i_\star = 114.5^{\circ\,+7.4}_{-10.0}$ and correspondingly the mass estimate of LHS 1610 b of $M = 49.5^{+4.3}_{-3.5}\ M_{\rm Jup}$. Despite the large scaling factor of $\sigma_{\rm scale} = 9.0^{+4.2}_{-2.5}$, the fractional uncertainty on the mass of LHS 1610 b is still at the ~7%–9% level, sufficient to conclude that the object is a brown dwarf.

Similar to Section 5.3.1, we assess the quality of the astrometric parameters through investigating the resulting Z-scores, which are highlighted in Figure 2. Figure 2 shows that increasing the uncertainties with $\sigma_{\rm scale}$ results in Z-scores which all have absolute values <1, suggesting that the sampled values are now in much better agreement given the updated uncertainties. Given the updated Z-scores and the agreement in the RV fit, we adopt these values as the formal parameters for LHS 1610 b.

We note that the adopted parameters assume that the joint-sampling methodology is able to give a good description of the parameters. As mentioned previously, we note that without having access to the underlying astrometric Gaia time series, it

is impossible to discern the exact cause of the underlying discrepancies. We urge the community to revisit this system and potentially other similar systems like it, to test the validity of this approach and the consistency of the final derived parameters.

6. Comparison to Other Brown Dwarf-M Dwarf Systems

LHS 1610 b joins a small but growing number of nearby brown dwarfs with precisely measured dynamical masses. Figure 3 puts LHS 1610 b in context with other known brown dwarf-M dwarf (BD-M) systems drawn from a compilation of objects with masses between 13 and 80 $M_{\rm Jup}$ from the NASA Exoplanet Archive (Akeson et al. 2013), the exoplanet.eu catalog, and the literature.

The top panel of Figure 3 shows the brown dwarf mass as a function of the distance of the system from Earth, where the points are color-coded by the host-star mass. We cut out systems that have a mass precision worse than 33%. We find LHS 1610 b to be the third-closest BD-M system within our mass-precision constraint. The other two more nearby targets are GJ 229 B (Brandt et al. 2021) and Scholz's Star B (Dupuy et al. 2019). Brandt et al. (2021) note that GJ 229 B is in tension with evolutionary models, as an object of its mass cannot cool to its luminosity within a Hubble time, suggesting it could instead be an unresolved binary (Howe et al. 2023).

By a statistical analysis of the brown dwarf population around FGK stars, Ma & Ge (2014) suggested that the brown dwarf population can be split into two regimes: the low-mass regime ($M < 42.5\ M_{\rm Jup}$), with an eccentricity distribution similar to gas giant planets, and a high-mass regime, with an eccentricity distribution similar to binary stars. With a mass of $49.5^{+4.3}_{-3.5}\ M_{\rm Jup}$, LHS 1610 b is formally in the high-mass regime discussed in Ma & Ge (2014), and therefore could have formed through molecular cloud fragmentation, similar to a binary stellar companion, as opposed to forming similar to a giant planet via gravitational instability or core accretion. However, in reality, the boundary between the two regimes is not exact, and is rather characterized by a "depletion region" between 35 and 55 M_J as discussed by Ma & Ge (2014), where short-period ($P < 100$ days) brown dwarfs are observed to be intrinsically rare. From its mass alone it is unclear which formation pathway LHS 1610 b would be more compatible with. Since the Ma & Ge (2014) study was performed on a sample of FGK stars, it may not be directly applicable to our BD-M dwarf binary. Further, the Ma & Ge (2014) study was focused on a sample of RV-discovered brown dwarfs, which only have minimum mass measurements ($m \sin i$), making it unclear if the "depletion region" discussed by Ma & Ge (2014) persists once true mass constraints are estimated. More discoveries of brown dwarfs that both have a RV and astrometric solutions will allow us to measure true masses for the brown dwarfs and more robustly determine if the "depletion region" persists in the brown dwarf population.

The faint points in both panels of Figure 3 show estimated values for the parameters of possible BD-M systems within 25 pc that have Gaia two-body solutions. The stellar masses are estimated by compiling the K magnitudes and using the Mann et al. (2019) mass–luminosity relation. Any object with an estimated stellar mass less than 0.65 $M_\odot$ is retained. Using the estimated stellar mass for these systems, we take the period, eccentricity, photocenter semimajor axis, parallax, and cosine of the inclination from the Gaia two-body solution and estimate the RV semi-amplitude, K, using Equation (13). With the stellar mass estimate and computed K, we estimate the mass of the companion under the assumption that the Gaia two-body solution correctly describes a single dark companion. These points highlight that Gaia is starting to uncover a number of additional candidate BD-M systems, allowing further insights into their occurrence rates and eccentricity distribution. However, as highlighted in this work as well as in Winn (2022), Halbwachs et al. (2023), and Marcussen & Albrecht (2023), precise RV follow-up observations are necessary to confirm that the two-body solutions are accurately describing the parameters of the systems, and to robustly rule out false-positive scenarios.

To further investigate LHS 1610 b's association with the planet or binary star formation pathways, Figure 3(B) compares the eccentricity and period of LHS 1610 b to other brown dwarfs. We see that LHS 1610 b has the highest eccentricity for confirmed systems with periods <10,000 days. Because of the short period and nonzero eccentricity, we may expect that tides will circularize LHS 1610 b's orbit (e.g., Mazeh 2008; Damiani & Díaz 2016). The companion will be circularized if its orbital period is less than the circularization period. M-dwarf binaries have an observed circularization period of ∼10 days (Udry et al. 2000; Mayor et al. 2001), while Sun-like binaries are ∼10–12 days (Duquennoy & Mayor 1991; Meibom & Mathieu 2005; Raghavan et al. 2010). The dashed line in Figure 3(B) indicates the maximum eccentricity a companion of a given period could have without experiencing tidal effects if the circularization period is 10 days (see Equation (3) in Halbwachs et al. 2005). With a period of $P = 10.6$ days and an eccentricity of $e = 0.37$, LHS 1610 b is inconsistent with both the aforementioned circularization period trends. Instead, LHS 1610 b fits a shorter circularization period of ∼8 days, more in line with the circularization periods of a few days observed for giant exoplanets (Halbwachs et al. 2005; Pont et al. 2011; Bonomo et al. 2017).

We estimate the circularization timescale to compare with our coarse estimate of the age of $7.0^{+4.5}_{-4.7}$ Gyr from the SED analysis. We use the Sonora–Bobcat models (Marley et al. 2021) to estimate the radius of the brown dwarf based on the mass and an age between 0.5 and 12 Gyr. Using the solar-metallicity models, at 0.5 Gyr we find a radius of 0.99 $R_{\rm Jup}$, and at 12 Gyr, 0.79 $R_{\rm Jup}$. We estimated the circularization timescale of the brown dwarf using Equations (1) and (2) from Jackson et al. (2008) and presented in Cañas et al. (2022) as

$$\frac{1}{\tau_e} = \frac{1}{\tau_{e,*}} + \frac{1}{\tau_{e,\rm BD}}, \tag{16}$$

$$\frac{1}{\tau_{e,*}} = a_{\rm BD}^{-13/2}\left(\frac{171}{16}\right)\sqrt{\frac{G}{M_*}}\frac{R_*^5 M_{\rm BD}}{Q_*}, \tag{17}$$

$$\frac{1}{\tau_{e,\rm BD}} = a_{\rm BD}^{-13/2}\left(\frac{63}{4}\right)\sqrt{GM_*^3}\frac{R_{\rm BD}^5}{Q_{\rm BD}M_{\rm BD}}, \tag{18}$$

where τ_e is the circularization timescale, $\tau_{e,*}$ is the timescale contribution from the star, and $\tau_{e,\rm BD}$ is the timescale contribution from the brown dwarf. The parameters $a_{\rm BD}$, M_*, $M_{\rm BD}$, R_*, $R_{\rm BD}$, Q_*, and $Q_{\rm BD}$ are the semimajor axis of the brown dwarf, the stellar host mass, the brown dwarf mass, the radius of the stellar host, the brown dwarf radius, and the tidal dissipation factors of the stellar host and brown dwarf, respectively. We assume a value of $Q_\star = 10^7$ based on

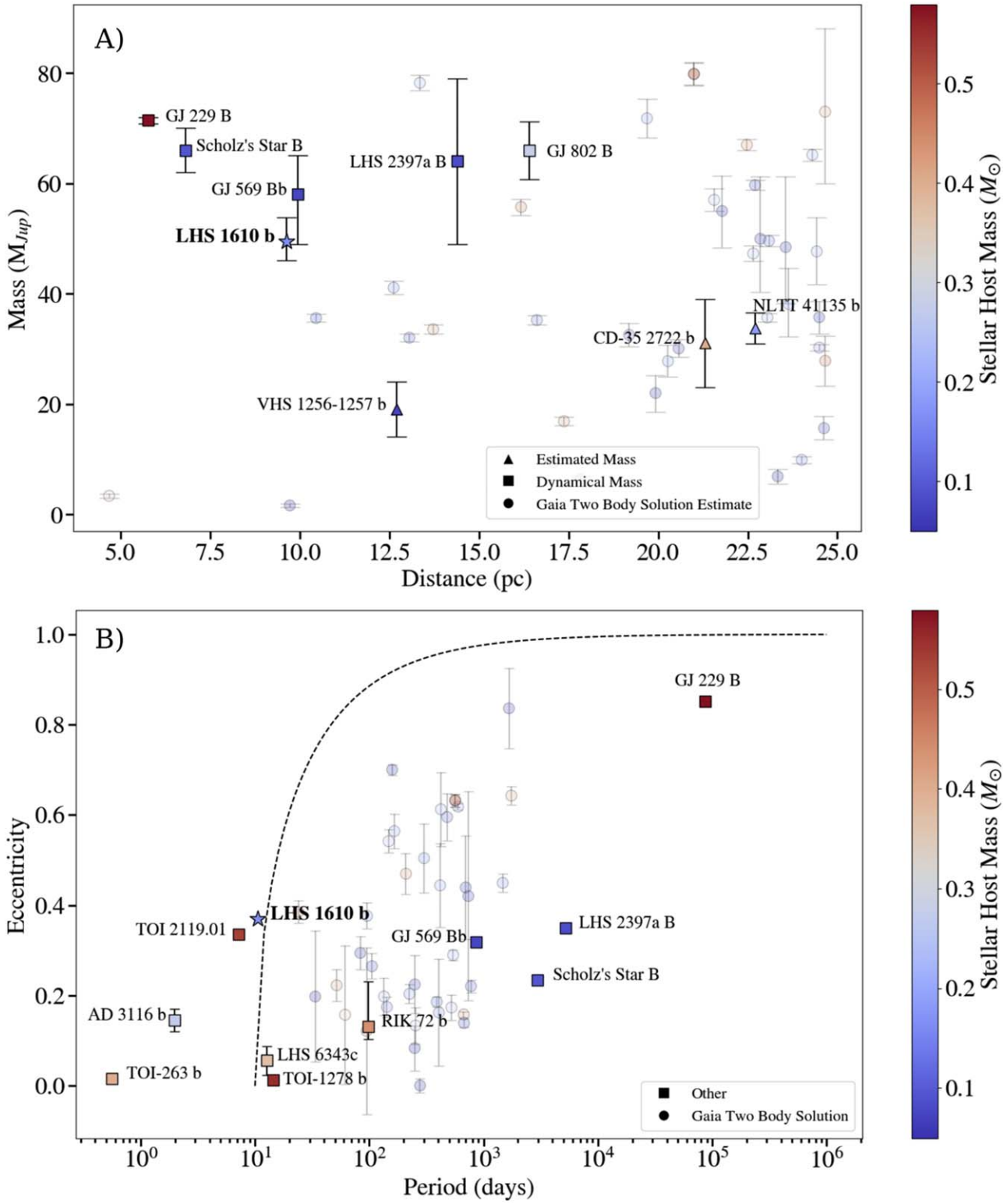

Figure 3. LHS 1610 b in context with other brown dwarfs orbiting M stars (BD-M systems). The colored points are confirmed BD-M star systems drawn from the NASA Exoplanet Archive, the exoplanet.eu catalog, and the literature. Not all systems have measurements for the plot parameters, so the points on each plot are individually labeled. To highlight the yield that Gaia will help enable, the fainter points show candidate BD-M systems from Gaia two-body solutions within 25 pc. Some errors are smaller than the marker size. Top (A): brown dwarf masses (better than 3σ) as a function of distance from Earth colored by the host-star mass. LHS 1610 b is the third most nearby BD-M system with a precise mass measurement. Bottom (B): same as above, but showing eccentricity as a function of orbital period in days. LHS 1610 b is one of the shortest-period BDs orbiting an M dwarf, and is the most eccentric in our sample besides GJ 229 B. The dashed line shows the expected eccentricity at a given period for a circularization period of 10 days. Similar to panel A, the fainter points show candidate BD-M systems from Gaia two-body solutions within 25 pc. The colored data points are available as the data behind the figure.

(The data used to create this figure are available in the online article.)

modeling done in Gallet et al. (2017) and $Q_{\rm BD} = 10^5$ as inferred for Jupiter (Goldreich & Soter 1966; Lainey et al. 2009; Lainey 2016). We assume the tidal dissipation factors remain constant over time, but in reality this factor will change as the star and brown dwarf evolve. For the 0.5 Gyr and 12 Gyr age assumptions, we obtain circularization timescales of 240 Gyr and 720 Gyr, respectively. The high circularization timescale we obtain in both cases suggests the system is not circularizing.

Additionally, we estimated the timescale for tidal synchronization using the equation from Guillot et al. (1996) and Rasio et al. (1996):

$$\tau_s = Q_{\rm BD}\left(\frac{R_{\rm BD}^3}{GM_{\rm BD}}\right)\omega_{\rm BD}\left(\frac{M_{\rm BD}}{M_\star}\right)^2\left(\frac{a_{\rm BD}}{R_{\rm BD}}\right)^6, \quad (19)$$

where $\omega_{\rm BD}$ is the primordial rotation rate of the brown dwarf. We again assume a value of $Q_{\rm BD} = 10^5$. For the primordial spin rate, Figure 13 of Tannock et al. (2021) shows measured rotation periods for 78 L, T, and Y dwarfs. Across spectral type, rotation periods between 1 and 10 hr are common. First, we will assume a rotation rate ($\omega_{\rm BD}$) of 10 hr (1.7×10^{-4} cycles per second), equal to that of Jupiter. For the 0.5 Gyr and 12 Gyr age assumptions, we obtain synchronization timescales of ∼7 Gyr and ∼15 Gyr, respectively. If we assume a rotation period of 1 hr instead (1.7×10^{-3} cycles per second), then our synchronization timescales for the 0.5 Gyr and 12 Gyr age assumptions are ∼70 Gyr and ∼150 Gyr, respectively. Although we note that the exact value is strongly dependent on the assumed primordial spin rate and tidal dissipation factor, the lengthy timescales indicated above suggest the brown dwarf has likely not become tidally locked.

7. Prospects for Star–Companion Interactions

Companions that closely orbit their host stars are thought to interact magnetically or sub-Alfvénically. These interactions are expected to enhance the activity of the host star, manifesting as enhanced X-ray and flaring activity (Lanza 2018; Ilin & Poppenhaeger 2022), radio emission (Zarka et al. 2001; Zarka 2007; Callingham et al. 2021; Kavanagh & Vedantham 2023), and chromospheric spots (Shkolnik et al. 2005). Furthermore, if the companion is magnetized, it may exhibit auroral emission due to the interactions between the stellar wind of the host star and its magnetosphere (Zarka et al. 2001). Signatures of these interactions in close-in exoplanetary systems are often loosely referred to as star–planet interactions. However, given that the companion of LHS 1610 is a brown dwarf, the term star–companion interactions is more appropriate.

To date, the magnitudes and scaling relationships of these interactions remain poorly constrained. Therefore, detections of objects compatible with such interactions are valuable laboratories to study such models. Due to the system's proximity, large size, and the short orbital period of the companion, LHS 1610 is a promising target for searching for possible evidence of star–companion interactions. We discuss this possibility in further detail in the following subsections.

7.1. Investigation of Potential Companion-induced Flaring

One way to look for evidence of sub-Alfvénic interactions is through looking for evidence of the phase dependence of flaring (e.g., Lanza 2018; Ilin & Poppenhaeger 2022) and/or orbital-phase-dependent variations in stellar activity indicators (e.g., Shkolnik et al. 2005), especially at orbital phases close to periastron. Examining the six visits of HPF observations, we see no evidence of emission in the Ca II infrared triplet activity indicators, and detect no hints of modulation as a function of orbital phase, and conclude that the star is not chromospherically active.

To constrain the possibility of flare-induced interactions in LHS 1610, we examined the three available sectors of TESS data of LHS 1610. To detect flares, we used the `stella` code (Feinstein et al. 2020a, 2020b), which leverages a set of trained convolutional neural networks to identify flares. To estimate a flare rate, we follow the methods outlined in Pope et al. (2021) and Medina et al. (2020), which we summarize briefly here. Using `stella`, we analyze the TESS 2 minutes cadence presearch data conditioning single-aperture photometry light curves using the `lightkurve` package (Lightkurve Collaboration et al. 2018) and apply a flare probability threshold of 0.6. To remove false positives, we follow Pope et al. (2021) and remove flares with (a) fractional amplitudes less than 3 times the standard deviation of a 400 minutes smoothed light curve, or (b) rise and fall times less than 4 minutes (two TESS cadences). After this step, sectors are reviewed by eye to add or remove any flares that were clearly misidentified.

Using this methodology, we detected a total of 17 flares: four in Sector 42, six in Sector 43, and seven in Sector 44 (see Figure 8 in Appendix A). From this, we estimate a flare rate of 0.28 ± 0.07 flares per day estimated using the total number of flares across the observing baseline covered by all three sectors. We estimate the 1σ uncertainty using a two-sided Poisson confidence interval. This flare rate is high given the star's rotation period when compared to a sample of nearby M stars with confirmed radio emission presented in Pope et al. (2021). LHS 1610 b has a flare rate similar to the M stars DO Cep and LP 259-39, which have substantially more rapid rotation periods of 0.41 day and 1.7 days, respectively.

To further investigate the possibility of flare-induced interactions, in Figure 4(A) we compare the flare rate of LHS 1610 as a function of rotation period from the volume-complete sample of mid-to-late M dwarfs within 15 pc from Medina et al. (2020) and Medina et al. (2022). By replicating their energy cutoff, completeness correction, and flare energy distribution, we see that LHS 1610 has a flare rate on the high end for its stellar rotation period of $P_{\rm rot} = 84.3 \pm 8$ days. The natural log of this flare rate is $\ln(R_{31.5}) = -2.51 \pm 0.45$ flares per day for flares above an energy of 3.16×10^{31} erg. We refer to this as the "high-energy" flare rate. In Figure 4(A), we highlight systems with confirmed substellar companions from the NASA Exoplanet Archive. Additionally, in Figure 4(A) we label in red systems with published radio detections that have been highlighted as potentially compatible with sub-Alfvénic interactions, including GJ 1151 (Vedantham et al. 2020; Callingham et al. 2021), Proxima Cen (Pérez-Torres et al. 2021), and YZ Ceti (Pineda & Villadsen 2023; Trigilio et al. 2023). Figure 4(A) shows that LHS 1610 joins those systems as an inactive, nearby M star with a longer rotation period, high optical flare rate, and a known companion. These similarities lead us to speculate that the brown dwarf may be inducing flares on LHS 1610. We evaluate the feasibility of observations that could be used to gain further insights into such interactions in the next section.

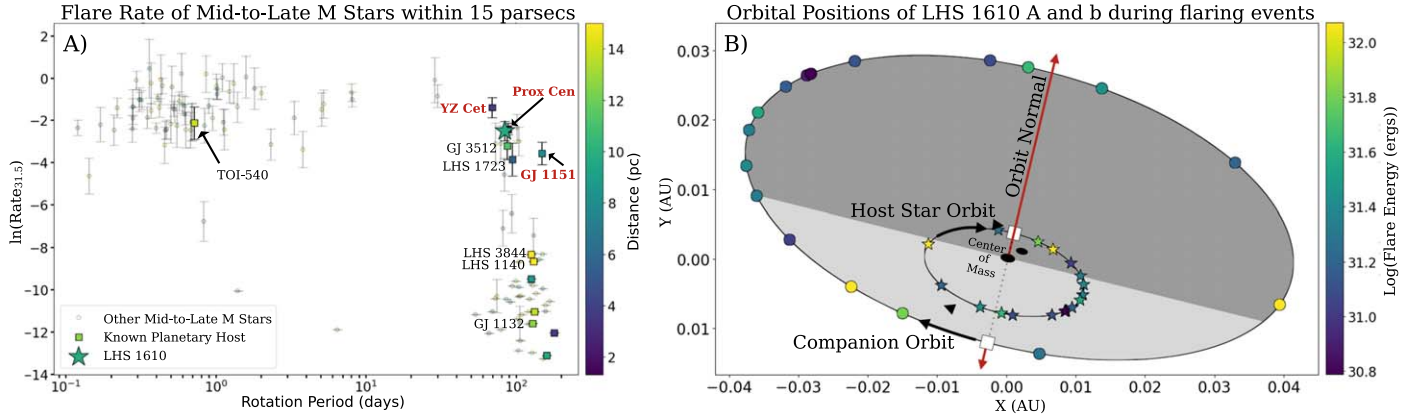

Figure 4. M-dwarf flare rates (A): log flare rate of flares with energies above the 3.16×10^{31} erg energy threshold discussed in Medina et al. (2022) as a function of stellar rotation period. Points are color-coded by distance to Earth. LHS 1610 is highlighted with the star. Systems with substellar companions are highlighted with black labels. Systems with published radio detections are highlighted in red. LHS 1610 joins a group of systems with high flare rates and long rotation periods. LHS 1610 flare orbital locations (B)**:** orbit visualization of the LHS 1610 b (outer ellipse) and its host star (inner ellipse) around the common center of mass using the joint Gaia-RV parameters from Table 2. The orbit is inclined ∼114° and the orbital direction is clockwise. The red vector denotes the orbit normal, and the periastron location is highlighted with the dotted line between the white squares. Locations of flares are highlighted twice per flare with the colored points, with a star/circle marker at the corresponding star/companion location. We do not see statistically significant evidence for a phase dependence of flare locations. The shaded regions define the intersection of the plane of the orbit with the plane of the sky along the line of nodes. The data shown in panel (B) are available as the data behind the figure. (The data used to create this figure are available in the online article.)

We further visualize the position of the flares in the orbit of LHS 1610 in Figure 4(B). Each flare along with its flare energy are shown both on the host-star orbit (star markers), as well as the position of the companion (circles). The flare energies are estimated following the same methodology as Medina et al. (2020). From Figure 4, we do not see any clear phase-dependent preference, including no clear preference for flaring close to periastron. In the half of the orbit encompassing periastron (phase values between −0.25 and 0.25 in Panel D of Figure 8) we find nine flares, which is consistent with the expectation of 8.6 ± 2.2 flares given our flare rate, suggesting there is no preference for flaring near periastron. We note that due to the low number of 17 flares detected, the Poisson counting uncertainties on the expected numbers of flares remain high. As such, additional flare monitoring to increase the total number of flare detections would be needed to provide conclusive evidence of any flare dependence in the system.

Lastly, brown dwarfs are known to have flares at comparable strengths to those observed around M stars (Gizis et al. 2017; Paudel et al. 2020), and some or all of the flares seen in the TESS photometry could be attributed to the brown dwarf. However, flaring brown dwarfs are generally young (<1 Gyr), and have spectral types earlier than L5 ($T_{\rm eff,L5} \sim 1800$ K). Using the Sonora–Bobcat models, we estimate the temperature of LHS 1610 b at the lower bound of our age estimate (2.5 Gyr) and find a value of ∼1100 K. Paired with the age estimate, LHS 1610 b seems unlikely to be the origin of the flares.

7.2. Stellar Wind Environment

For sub-Alfvénic interactions to occur, the companion must orbit sub-Alfvénically, i.e., with an Alfvénic Mach number ($M_{\rm A}$) less than unity (Saur et al. 2013):

$$M_{\rm A} = \Delta u / u_{\rm A} < 1. \tag{20}$$

Here, Δu is the relative velocity of the stellar wind as seen by the orbiting planet:

$$\Delta \vec{u} = \vec{u}_{\rm w} - \vec{u}_{\rm orb}, \tag{21}$$

where $u_{\rm w}$ is the wind velocity, and $u_{\rm orb}$ is the orbital velocity of the brown dwarf. $u_{\rm A}$ is the Alfvén speed,

$$u_{\rm A} = \frac{B_{\rm w}}{\sqrt{4\pi\rho_{\rm w}}}, \tag{22}$$

where $B_{\rm w}$ and $\rho_{\rm w}$ are the magnetic field strength and the mass density of the stellar wind, respectively. Therefore, knowing how both of these quantities vary as a function of distance, along with the wind velocity, is required to determine if a companion orbits sub-Alfvénically.

The wind densities of low-mass main-sequence stars like LHS 1610 are notoriously difficult to detect given their rarefied nature, and current measurements are both indirect and few in number. A way to quantify stellar wind densities is through their mass-loss rate:

$$\dot{M} = 4\pi r^2 \rho_{\rm w} u_{{\rm w},r}, \tag{23}$$

where r the is distance from the star, and $u_{{\rm w},r}$ is the wind velocity in the radial direction. Wood et al. (2021) presented the most up-to-date list of mass-loss rate estimates for low-mass main-sequence stars. For M dwarfs, these values vary from 0.06 to 200 $\dot{M}_\odot$, where $\dot{M}_\odot = 2 \times 10^{-14}\, M_\odot\ {\rm yr}^{-1}$ is the mass-loss rate of the Sun (Cohen 2011). In the absence of a measured mass-loss rate for LHS 1610, we adopt this range of values.

Stellar winds from low-mass main-sequence stars are thought to be predominantly driven by the thermal expansion of a hot corona (Gombosi et al. 2018). Therefore, estimating the temperature of their coronae can provide constraints on the velocity of the wind. Johnstone & Güdel (2015) found the following empirical relation between the observed surface X-ray flux (F_X) and inferred coronal temperatures ($T_{\rm corona}$) of these stars:

$$T_{\rm corona} = 0.11 F_X^{0.26} \times 10^6\ {\rm K}, \tag{24}$$

where F_X is in $10^6\ {\rm erg\ s^{-1}\ cm^{-2}}$. Note that the errors in the fit coefficients in Equation (24) are less than 1%.

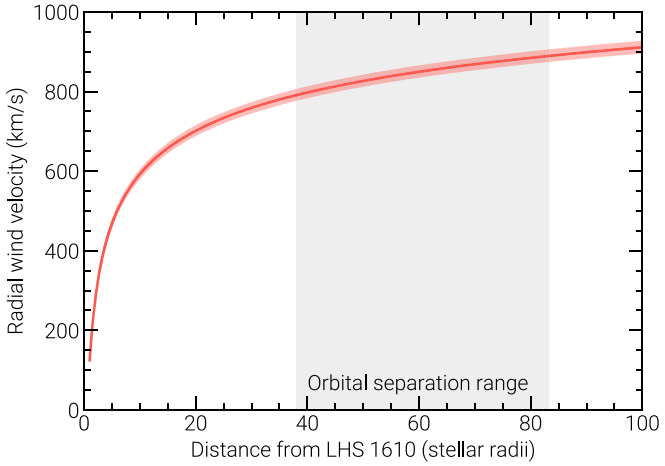

Figure 5. The radial wind velocity profile estimated for LHS 1610. The red shaded region shows the 1σ uncertainty. The range of orbital separations between the brown dwarf and host star is shown by the gray shaded region. During its orbit, the brown dwarf is subjected to stellar wind velocities of ~800 to 900 km s^{-1}.

Magaudda et al. (2020) reported an X-ray luminosity for LHS 1610 of $L_X = 10^{26.94\pm0.04}$ erg s^{-1} from observations with the Chandra X-ray Observatory (Weisskopf et al. 2000; Wright & Drake 2016; Wright et al. 2018). Converting this value to the surface X-ray flux ($F_X = L_X/4\pi {R_\star}^2$), we estimate a coronal temperature for LHS 1610 via Equation (24) of $(3.05 \pm 0.07) \times 10^6$ K.

Models for thermally driven stellar winds have existed for decades, the first of which being proposed by Parker (1958). Despite its simplicity, it reproduces the bulk properties of the solar wind remarkably well. While more sophisticated models exist, they are both computationally expensive and dependent on information that is often not readily available, such as the surface magnetic field topology (e.g., Kavanagh et al. 2022). Again, in the absence of such information for LHS 1610, we opt for a simple prescription to estimate its wind velocity profile. For this, we use the code developed by Kavanagh & Vidotto (2020), which produces the radial wind velocity profile $u_{w,r}$ described by Parker (1958) for a given stellar mass and coronal temperature. We show our estimated velocity profile in Figure 5. We find that over the course of its orbit, the companion is subject to wind speeds of around 800 to 900 km s^{-1}.

The wind velocity solution described by Parker (1958) is purely radial in direction. Such a scenario is expected for a star like LHS 1610 given its slow rotation (Preusse et al. 2005; Johnstone 2017). Similarly, it is expected to have a large-scale magnetic field that is predominantly radial. To validate this, we take the wind model for the star Proxima Centauri presented by Kavanagh et al. (2021), and compute the radial component of the wind velocity and magnetic field, as well as the fraction of the large-scale magnetic field that is open, as a function of distance. This is shown in Appendix B. We choose Proxima Centauri given both its similarities to LHS 1610 (Section 7.1) and also since we lack a mass-loss rate estimate and the magnetic field topology of the star (unlike Proxima). We find that the wind velocity and magnetic field are predominantly radial at a distance greater than around 10 stellar radii (R_*) for Proxima Centauri. This is also consistent with an open magnetic field geometry.

Knowing the geometry of the large-scale magnetic field is important for estimating signatures of possible star–companion interactions, as we will see in the following sections. For an open-field geometry, magnetic flux conservation gives us the following scaling for the magnetic field of the wind:

$$B_w = \langle B_V \rangle \left(\frac{R_\star}{r}\right)^2. \quad (25)$$

Here, $\langle B_V \rangle$ is the unsigned average large-scale magnetic field strength at the stellar surface. This is the most relevant quantity in terms of what drives the stellar wind outflow (Jardine et al. 2017; Vidotto 2021).

The Zeeman Doppler imaging method (ZDI) can provide estimates for $\langle B_V \rangle$. Recently, Klein et al. (2021), Bellotti et al. (2023), and Lehmann et al. (2024) used ZDI to estimate magnetic field strengths for slowly rotating M dwarfs like LHS 1610 for the first time. These stars, all with rotation periods exceeding 40 days, exhibit predominantly dipolar magnetic fields, with strengths ranging from $\langle B_V \rangle = 16$ to 214 G. We adopt this range of values for LHS 1610. We note that Henry et al. (2018) illustrated LHS 1610 may be undergoing magnetic cycles. However, the values used here from Lehmann et al. (2024) include those for stars exhibiting magnetic variability and long-term activity cycles. Therefore, any variability in the large-scale surface magnetic field of LHS 1610 should be encoded within the range of values adopted here.

With the wind velocity profile, mass-loss rate, and magnetic field of LHS 1610 estimated, we now compute the Alfvén velocity via Equation (22). The density profile is obtained from Equation (23). Note that since the orbital velocity vector of the brown dwarf is perpendicular to the radial direction, and the wind velocity is in the radial direction, the relative velocity between the wind and the orbit of the brown dwarf is $\Delta u = \sqrt{{u_{w,r}}^2 + {u_{BD}}^2}$. With this, we then compute the Alfvénic Mach number via Equation (20).

Given that the separation between the star and its companion varies significantly over the orbit, we compute the fraction of the orbit where the companion is sub-Alfvénic as a function of the mass-loss rate and magnetic field strength at the surface. This is shown in Figure 6. We see that sub-Alfvénic interactions are possible, provided the wind mass-loss rate is low enough and the surface magnetic field is strong enough. However, currently we do not have sufficient statistics for M dwarfs to estimate the probability density of the mass-loss rate and surface field strength for LHS 1610, and therefore cannot determine the likelihood that it has conditions sufficient to drive sub-Alfvénic interactions. The necessity of the surface magnetic field measurement to study star–companion interations motivates follow-up observations to derive the surface magnetic field of the star via the ZDI method.

7.3. Sub-Alfvénic Interactions between LHS 1610 b and Its Host Star

If LHS 1610 b is in a sub-Alfvénic orbit, it could enhance emission on the host star at a wide range of wavelengths by the dissipation of energy carried by Alfvén waves generated via sub-Alfvénic interactions (Zarka 2007; Saur et al. 2013). The power produced via these interactions is (Saur et al. 2013;

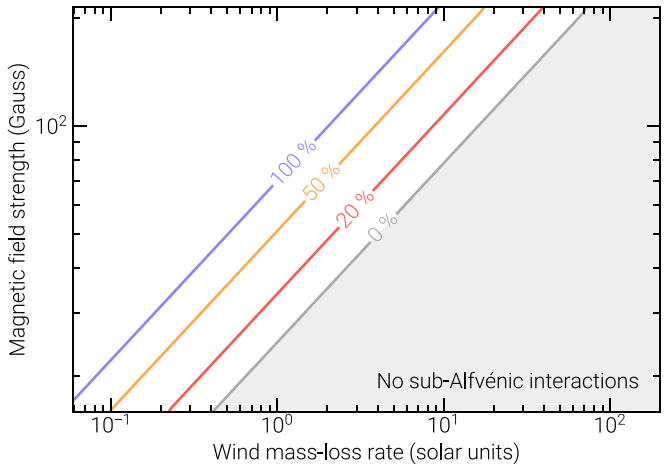

Figure 6. The fraction of the orbit that LHS 1610 b orbits sub-Alfvénically as a function of the stellar wind mass-loss rate and unsigned average large-scale surface magnetic field of the host star. The gray shaded region shows where sub-Alfvénic interactions are not possible. Provided the mass-loss rate is sufficiently low and the surface magnetic field is sufficiently strong, the brown dwarf can magnetically interact with the host star, enhancing the star's activity.

Kavanagh et al. 2022)

$$P_{\rm SA} = \pi^{1/2} {R_{\rm obs}}^2 B_{\rm w} {\rho_{\rm w}}^{1/2} \Delta u^2 \sin^2\theta, \quad (26)$$

where $R_{\rm obs}$ is the size of the obstacle perturbing the stellar magnetic field, and θ is the angle between the relative velocity and magnetic field vectors $\Delta\vec{u}$ and $\vec{B}_{\rm w}$. As shown in Section 7.2, the magnetic field of the wind likely points in the radial direction (i.e., θ is also the angle between $\Delta\vec{u}$ and the wind velocity vector $\vec{u}_{\rm w}$). In the case that LHS 1610 b is unmagnetized, $R_{\rm obs}$ is simply its radius, $R_{\rm BD}$. However, if it possesses an intrinsic magnetic field, the size of the obstacle is the size of its magnetosphere, $R_{\rm M}$. This can be estimated by computing the magnetopause distance, the point where the pressure of the incident stellar wind balances with the pressure exerted by the magnetic field of LHS 1610 b (Vidotto et al. 2012):

$$R_{\rm M} = \left(\frac{{B_{\rm BD}}^2}{32\pi p_{\rm w}}\right)^{1/6} R_{\rm BD}. \quad (27)$$

Here, $B_{\rm BD}$ is the field strength of LHS 1610 b at its magnetic poles, assuming the field is dipolar, and $p_{\rm w}$ is the pressure of the stellar wind at its orbit:

$$p_{\rm w} = \rho_{\rm w}(a^2 + \Delta u^2) + \frac{{B_{\rm w}}^2}{8\pi}, \quad (28)$$

where $a = \sqrt{2kT/m_p}$ is the isothermal sound speed.

As there are no published detections of radio aurorae from LHS 1610 b, we cannot estimate its magnetic field strength directly (Kao et al. 2018). Therefore, we use the following theoretical prescription for the magnetic field strength from Reiners & Christensen (2010) to estimate the dipolar magnetic field strength of LHS 1610 b:

$$B_{\rm BD} = 3.39\left(\frac{M_{\rm BD}{L_{\rm BD}}^2}{{R_{\rm BD}}^7}\right)^{1/6} \text{kG}, \quad (29)$$

where $M_{\rm BD}$, $R_{\rm BD}$, and $L_{\rm BD}$ are the mass, radius, and luminosity of the brown dwarf, respectively. Note that this relation assumes that the brown dwarf is rotating sufficiently fast, which is likely for LHS 1610 b given its long synchronization time (Section 6).

Table 3
Physical Parameters Estimated for LHS 1610 b as a Function of Age

Age (Gyr)	$R_{\rm BD}$ ($R_{\rm Jup}$)	$\log L_{\rm BD}$ ($L_\odot$)	$B_{\rm BD}$ (G)	$R_{\rm M}$ ($R_{\rm Jup}$)
2	0.86 ± 0.01	$-4.88^{+0.12}_{-0.10}$	816^{+98}_{-78}	$9.67^{+1.67}_{-0.78}$ –$12.50^{+2.50}_{-1.06}$
7	0.80 ± 0.01	$-5.63^{+0.11}_{-0.09}$	495^{+61}_{-46}	$7.67^{+1.34}_{-0.61}$ –$9.91^{+2.00}_{-0.83}$
12	0.79 ± 0.01	$-5.93^{+0.11}_{-0.08}$	402^{+48}_{-35}	$7.02^{+1.23}_{-0.56}$ –$9.07^{+1.83}_{-0.76}$

Notes. The radius $R_{\rm BD}$ and luminosity $L_{\rm BD}$ are obtained via our estimate for the mass of $49.5^{+4.3}_{-3.5}$ $M_{\rm Jup}$ using the isochrones from Marley et al. (2021). We then use these to compute the dipole strength $B_{\rm BD}$ via Equation (29). Combined with the estimated stellar wind parameters, we estimate the range of sizes for the brown dwarf's magnetosphere $R_{\rm M}$, which varies over its orbit due to the eccentricity. The lower and upper limits correspond to the values computed at periastron and apastron, respectively.

The radius and luminosity of brown dwarfs can be estimated from isochrones if its mass and age are known. However, the uncertainty on the age of the system is large. Therefore, we consider three ages of 2, 7, and 12 Gyr for LHS 1610 b. We draw samples for the mass of the brown dwarf from the constraint obtained in Section 5.3.2, and linearly interpolate for the radius and luminosity from the the solar-metallicity isochrones provided by Marley et al. (2021) at the three ages listed above. In this age range, we find radii of 0.86 to 0.79 $R_{\rm Jup}$, and luminosities of -4.88 to -5.93 $L_\odot$ in log-space, where $L_\odot$ is the luminosity of the Sun ($L_\odot = 3.83 \times 10^{33}$ erg s^{-1}; Vieira et al. 2022).

With the radius and luminosity estimated, we now use Equation (29) to estimate the field strength for LHS 1610 b. For this, we find strengths of 816–402 G, which are up to an order of magnitude larger than the field strengths estimated for M dwarfs similar to LHS 1610. This is unsurprising however, as the star likely rotates much slower than the brown dwarf. Having estimated the radius and field strength of the brown dwarf, we finally can estimate the size of its magnetosphere via Equation (27) in combination with the estimated stellar wind properties. We find large sizes, ranging from around 7 to 13 $R_{\rm Jup}$ depending on the age and orbital phase. The inferred parameters and their uncertainties as a function of age are listed in Table 3.

With both the estimates for the properties of the stellar wind and the obstacle size of the brown dwarf established, we now use Equation (26) to estimate the power dissipated along the stellar magnetic field via sub-Alfvénic interactions. We uniformly sample the mass-loss rate and unsigned large-scale surface magnetic field strength in the aforementioned ranges adopted for LHS 1610. We also consider the cases where LHS 1610 b is both magnetized and weakly/unmagnetized (i.e., $R_{\rm obs} \approx R_{\rm BD}$ in Equation (26)).

In Figure 7, we show the estimated power generated via sub-Alfvénic interactions between the brown dwarf and stellar magnetic field as a function of orbital phase, for an age of 7 Gyr. For the magnetized case, we estimate the total power produced to be within the range of $\sim 10^{24}$–10^{25} erg^{-1}, whereas in the unmagnetized case, it ranges from $\sim 10^{22}$ to 10^{23} erg^{-1}. Due to the eccentricity of the orbit, the distance between the two bodies varies from 38 to 83 $R_\star$ over the course of the orbit.

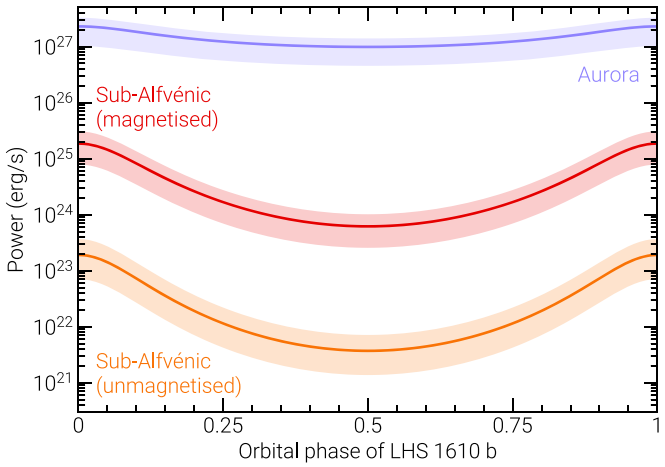

Figure 7. Estimated powers from both sub-Alfvénic interactions between LHS 1610 b and its host star (red and orange curves), and auroral emission from the brown dwarf's magnetosphere due to the incident stellar wind (purple curves). Each solid line and shaded region shows the median and the 1σ region, respectively. The powers are shown as a function of orbital phase, which are modulated due to the eccentricity of the orbit. For the sub-Alfvénic powers, we show the cases where the brown dwarf is both magnetized (red curves) and unmagnetized (orange curves). The powers are computed assuming an age of 7 Gyr for the brown dwarf. The differences in the curves at the ages of 2 and 12 Gyr are small, as the radius of the brown dwarf does not change significantly, and the size of its magnetosphere varies weakly with the magnetic field strength (see Equation (27)). In all cases, a fraction of the energy (10^{-4}–10^{-2}) is expected to be released at radio wavelengths, resulting in flux estimates that are within reach of sensitive radio telescopes such as LOFAR and the VLA. Note that the sub-Alfvénic interaction scenario is only possible provided the host star has a sufficiently low mass-loss rate and strong surface magnetic field (see Figure 6).

As a result, the brown dwarf is subjected to time-varying stellar wind conditions. Therefore, the power dissipated onto the star also varies, as is seen in the light curves in Figure 7.

If the estimated power generated by sub-Alfvénic interactions, $P_{\rm SA}$, is indeed dissipated onto the star's magnetic field, some fraction is expected to manifest as bright radio emission via the electron cyclotron maser (ECM) instability (Zarka 2007; Saur et al. 2013). For the Io-induced emission on Jupiter, this fraction or "efficiency ratio" η is estimated to be around 10^{-4}–10^{-2} (Turnpenney et al. 2018; Saur et al. 2021). If we assume this fraction of the total power is uniformly dissipated in the radio over the frequency range $\Delta\nu$, the flux density observed at a distance d is

$$F_\nu = \frac{\eta P_{\rm SA}}{d^2 \Omega_{\rm beam} \Delta\nu}, \tag{30}$$

where $\Omega_{\rm beam}$ is the solid angle of the emission beam, which is a hollow cone since ECM emission is beamed. Typical values assumed for Ω range from 0.16 to 1.6 sr (Zarka et al. 2004; Turnpenney et al. 2018). If the frequency range $\Delta\nu$ is sufficiently wide, it is effectively equal to the cutoff frequency $\nu_{\rm max}$, which we assume to be that at the stellar surface. Given that ECM emission occurs at the local cyclotron frequency (Dulk 1985), the cutoff frequency is therefore the cyclotron frequency at the surface:

$$\nu_{\rm max} = 2.8 \langle B_V \rangle \ {\rm MHz}, \tag{31}$$

where $\langle B_V \rangle$ is the unsigned surface average field strength in units of gauss.

Let us consider a conservative scenario, in which $\eta = 10^{-6}$ and $\Omega = 1.6$ sr. For the unmagnetized and magnetized cases, the sub-Alfvénic radio fluxes produced can reach up to 0.6 mJy and 60 mJy, respectively. The emission frequency varies from 45 to 600 MHz based on the estimated surface field strength. Emission in this range at a millijansky level is well within the capabilities for detection with radio telescopes such as LOFAR and the Giant Metrewave Radio Telescope (see Callingham et al. 2021; Narang et al. 2021). Therefore, LHS 1610 is a compelling case for follow-up searches in the radio for signatures of sub-Alfvénic interactions.

We note also that since ECM emission is beamed, the visibility of the radio emission is highly dependent on the underlying system geometry (e.g., Kavanagh et al. 2022; Kavanagh & Vedantham 2023). By combining the orbital characteristics derived in this work with efforts to map the surface magnetic field topology via ZDI (e.g., Klein et al. 2021), we could estimate at what orbital phases we would expect to see the radio emission. In addition to potential radio emission, signatures of sub-Alfvénic interactions occurring in the system may be visible at different wavelengths such as in the optical (see Section 7.1), ultraviolet (UV), and infrared (Shkolnik et al. 2005; Klein et al. 2022).

7.4. Auroral Emission from LHS 1610 b

Regardless of whether LHS 1610 b is in a sub-Alfvénic orbit or not, if it possesses an intrinsic magnetic field it may also exhibit strong auroral emission produced via the dissipation of the energy carried by the stellar wind onto its magnetosphere (Zarka 2007). For the magnetized bodies in the solar system, their observed auroral emission at radio wavelengths scales linearly with the solar wind power intercepted by their magnetospheres. The power intercepted is (Zarka 2007)

$$P_{\rm aurora} = \varepsilon \Delta u \pi R_{\rm M}{}^2, \tag{32}$$

where $\varepsilon = \varepsilon_{\rm kin} + \varepsilon_{\rm mag} + \varepsilon_{\rm th}$ is the energy density of the incident wind, which is comprised of a kinetic, magnetic, and thermal component:

$$\varepsilon_{\rm kin} = \rho_{\rm w} \Delta u^2, \tag{33}$$

$$\varepsilon_{\rm mag} = \frac{B_{\rm w}^2 \sin^2\theta}{4\pi}, \tag{34}$$

$$\varepsilon_{\rm th} = a^2 \rho. \tag{35}$$

In the solar system, generally only the kinetic and thermal components are considered, which both appear to produce powers that are directly proportional to the observed auroral radio power, with around 10^{-5} to 10^{-3} of the incident power being dissipated (Zarka 2007). For completeness, we also include the thermal energy incident on the magnetosphere (Elekes & Saur 2023). In a similar manner to Section 7.3, we compute the incident power on the magnetosphere of LHS 1610 b as a function of its orbital phase, varying $\dot{M}$ and $\langle B_V \rangle$ over the assumed ranges for the host star. This is shown in Figure 7 alongside the powers estimated in Section 7.3 from sub-Alfvénic interactions. We again find large powers of around $\sim 10^{27}$ erg^{-1}. Note that accounting for the surface magnetic field of the host star will introduce further modulation to the powers shown in Figure 7 (e.g., Kavanagh et al. 2022). Additionally, we assume the rotation and magnetic axes of the brown dwarf are aligned with the star's rotation axis. Varying the orientation of these axes could also modulate power for

these interactions, in that it will alter how the magnetic fields of the wind and the brown dwarf interact. Accounting for this, however, would require a full 3D magnetohydrodynamics simulation, which is beyond the scope of this work.

We now compute the radio flux via Equation (30), replacing P_{SA} with P_{aurora}. We again choose conservative values for $\eta = 10^{-6}$ (an order of magnitude lower than the minimum value estimated for auroral radio emission in the solar system) and $\Omega = 1.6$ sr. We set the cyclotron frequency at the magnetic poles of the brown dwarf as the cutoff frequency, as the field lines on which the aurora is driven likely connect back near the magnetic poles due to the large size of its magnetosphere. At an age of 7 Gyr, this frequency is ∼1.4 GHz. We find that, with these estimates, the flux density should be of the order of ∼200 mJy. At GHz frequencies, the Very Large Array (VLA) would be suitable for follow-up observations (e.g., Villadsen & Hallinan 2019), which to date has been the primary telescope used to discover radio emission from brown dwarfs (Tang et al. 2022). This highlights the benefit of carrying out a multiwavelength radio campaign of the system, in that we could determine if sub-Alfvénic interactions and/or aurorae could be detected by observing at both MHz and GHz frequencies. Such observations could constrain both the sub-/super-Alfvénic nature of the companion, and also the field strengths of both objects. Again, the visibility of this emission is dependent on the geometry of the brown dwarf's magnetic field, which is unknown. However, the auroral signature should appear at specific rotation phases (Pineda et al. 2017), unlike stochastic flares from the star, which should have no preferential phase. Auroral emission is also a possibility at other wavelengths. If the brown dwarf was isolated, prospects for detecting its aurora would likely be most favorable at UV wavelengths (Saur et al. 2021).

8. Summary

We studied the LHS 1610 system, a nearby M5 dwarf ($d = 9.7$ pc) hosting a brown dwarf in a short-period ($P = 10.6$ days), eccentric ($e = 0.37$) orbit. This system is the second-closest M dwarf with a substellar companion and a Gaia two-body solution behind GJ 876, an M-dwarf system hosting at least four known planets, and LHS 1610 b is the most eccentric brown dwarf orbiting an M dwarf behind GJ 229 B.

Jointly modeling the available RVs from HPF and TRES with the Gaia two-body solution, we are able to make new estimates for all of the orbital elements of LHS 1610 b. We obtain an orbital inclination of $i_\star = 114.5^{\circ +7.4}_{-10.0}$, resulting in a mass estimate of $M = 49.5^{+4.3}_{-3.5}\,M_{\rm Jup}$, confirming the brown dwarf nature of the companion. We highlight the discrepancy between the RV-only fit eccentricity ($e = 0.37$) and that of the Gaia two-body solution ($e = 0.52$). To account for this discrepancy, we include an uncertainty scaling factor in the astrometric covariance matrix that inflates the overall errors. We note the necessity to revisit this system when the astrometric data are released in Gaia Data Release 4.

Due to LHS 1610 b's large radius and close-in orbit around its host star, LHS 1610 b is a promising target for the detection of potential sub-Alfvénic interactions at a wide range of wavelengths. Using the available TESS data, we derive a flare rate of 0.28 ± 0.7 flares per day. When accounting for a flare energy cutoff ($E > 10^{31.5}$), the subsequent flare rate places LHS 1610 among the high end for its rotation period among a volume-complete sample of mid-to-late M stars within 15 pc from Medina et al. (2020) and Medina et al. (2022). Within this sample, LHS 1610 is similar in spectral type, flare rate, and rotation period to Proxima Centauri and YZ Ceti, both of which have observed radio emission attributed to possible sub-Alfvénic interactions. Using the available TESS data for LHS 1610, we detected no significant phase dependence of the flares, and highlight that additional data would be needed to decisively confirm or rule out such a dependence.

We simulated the expected energetics of both sub-Alfvénic interactions and auroral emission from the brown dwarf. For the sub-Alfvénic interactions, we demonstrate that LHS 1610 b may reside in a sub-Alfvénic orbit over its variable range of orbital distances due to its eccentricity, a necessary requirement to support sub-Alfvénic interactions. We show that, given even conservative estimates, the radio emission expected from the star due to these interactions is within the sensitivity range of LOFAR and other radio instruments. Additionally, we show that direct auroral emission from the brown dwarf could be even more easily detectable than the radio emission from sub-Alfvénic interactions, with nominal expected radio powers in in the 10^{24}–10^{26} erg s^{-1} range. The detection of either of these interactions is dependent on the orbital phase of the brown dwarf, which benefit from the full orbital solution and precise ephemeris provided in Table 2.

This work provides an outline for leveraging a fully characterized orbital solution to study star–planet/star–companion interactions. This will be useful as more systems like LHS 1610 are discovered and characterized jointly by Gaia astrometry and precise ground-based radial velocities.

Acknowledgments

We thank the anonymous referee for their thoughtful comments and suggestions that improved the quality of the manuscript. G.S. acknowledges support provided by NASA through the NASA Hubble Fellowship grant No. HST-HF2-51519.001-A awarded by the Space Telescope Science Institute, which is operated by the Association of Universities for Research in Astronomy, Inc., for NASA, under contract NAS5-26555. R.D.K. acknowledges funding from the Dutch Research Council (NWO) for the e-MAPS (Exploring Magnetism on the Planetary Scale) project (project number VI.Vidi.203.093) under the NWO talent scheme Vidi. We acknowledge support form NASA XRP Grant 80NSSC24K0155.

This work was partially supported by funding from the Center for Exoplanets and Habitable Worlds. The Center for Exoplanets and Habitable Worlds is supported by the Pennsylvania State University, the Eberly College of Science, and the Pennsylvania Space Grant Consortium. C.I.C. acknowledges support by NASA Headquarters through an appointment to the NASA Postdoctoral Program at the Goddard Space Flight Center, administered by ORAU through a contract with NASA. This work was performed for the Jet Propulsion Laboratory, California Institute of Technology, sponsored by the United States Government under the Prime Contract 80NM0018D0004 between Caltech and NASA. We acknowledge support from NSF grants AST-1909506, AST-190950, AST-1910954, and AST-1907622. Computations for this research were performed on the Pennsylvania State University's Institute for Computational & Data Sciences (ICDS).

These results are based on observations obtained with the Habitable-zone Planet Finder Spectrograph on the HET. We acknowledge support from NSF grants AST 1006676, AST 1126413, AST 1310875, and AST 1310885, and the NASA

Astrobiology Institute (grant No. NNA09DA76A) in our pursuit of precision radial velocities in the NIR. We acknowledge support from the Heising-Simons Foundation via grant 2017-0494. This research was conducted in part under NSF grants AST-2108493, AST-2108512, AST-2108569, and AST-2108801 in support of the HPF Guaranteed Time Observations survey. The Hobby–Eberly Telescope is a joint project of the University of Texas at Austin, the Pennsylvania State University, Ludwig-Maximilians-Universitat Munchen, and Georg-August Universitat Gottingen. The HET is named in honor of its principal benefactors, William P. Hobby and Robert E. Eberly. The HET collaboration acknowledges the support and resources from the Texas Advanced Computing Center. We thank the resident astronomers and telescope operators at the HET for the skillful execution of our observations with HPF.

B.J.S.P. acknowledges and pays respect to the traditional owners of the land on which the University of Queensland is situated, and to their ancestors and descendants, who continue cultural and spiritual connections to the country.

This research has made use of data obtained from or tools provided by the portal exoplanet.eu of The Extrasolar Planets Encyclopaedia.

This work has made use of data from the European Space Agency (ESA) mission Gaia (https://www.cosmos.esa.int/gaia), processed by the Gaia Data Processing and Analysis Consortium (DPAC; https://www.cosmos.esa.int/web/gaia/dpac/consortium). Funding for the DPAC has been provided by national institutions, in particular the institutions participating in the Gaia Multilateral Agreement.

This research made use of Astropy, a community-developed core Python package for Astronomy (Astropy Collaboration et al. 2013).

We acknowledge the Texas Advanced Computing Center (TACC) at The University of Texas at Austin for providing high-performance computing, visualization, and storage resources that have contributed to the results reported within this paper.

TESS data presented in this paper were obtained from the Mikulski Archive for Space Telescopes (MAST) at the Space Telescope Science Institute. The specific observations analyzed can be accessed via 10.17909/fwdt-2x66 and 10.17909/t9-nmc8-f686. STScI is operated by the Association of Universities for Research in Astronomy, Inc., under NASA contract NAS5-26555. Support to MAST for these data is provided by the NASA Office of Space Science via grant NAG5-7584 and by other grants and contracts.

This work makes use of the NASA Exoplanet Archive (2023), which is maintained by the NASA Exoplanet Science Institute at IPAC, which is operated by the California Institute of Technology under contract with the National Aeronautics and Space Administration.

Facilities: HET, FLWO:1.5m, TESS, Gaia

Software: `astropy` (Astropy Collaboration et al. 2013), `barycorrpy` (Kanodia & Wright 2018), `corner.py` (Foreman-Mackey 2016), `emcee` (Foreman-Mackey et al. 2013), `Jupyter` (Kluyver et al. 2016), `matplotlib` (Hunter 2007), `numpy` (Van Der Walt et al. 2011), `pandas` (McKinney 2010), `pyde` (Parviainen 2016), `radvel` (Fulton et al. 2018), `SERVAL` (Zechmeister et al. 2018), `HxRGproc` (Ninan et al. 2018).

Appendix A
Transiting Exoplanet Survey Satellite Flares

We show the TESS photometry in Figure 8 and highlight the flares identified from our analysis using the `stella` (Feinstein et al. 2020a) flare-finding algorithm. The flares are highlighted by vertical gray bars. Points are color-coded by the flare probability assigned by `stella`, where red points have a probability greater than 0.6 and gray points are those below

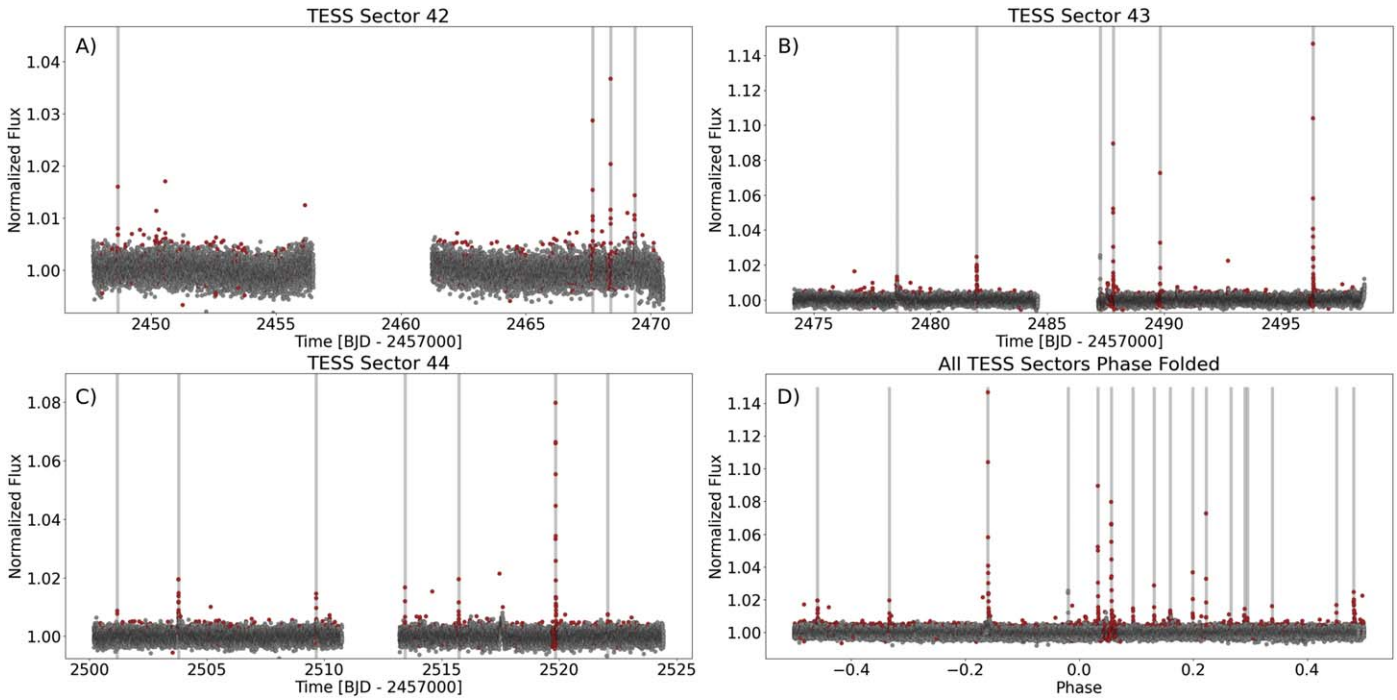

Figure 8. Flares in TESS photometry. Panels A, B, and C show individual sector light curves for TESS Sectors 42, 43, and 44, respectively. Points are colored by flare probability assigned by `stella`; red show a probability >60%, and gray points a probability <60%. Flares that passed our cuts are highlighted by the vertical gray bars. Panel D contains the combination of all sectors phase-folded on the period centered on the time of periastron. Flares are again highlighted by vertical gray bars. We do not see statistically significant evidence for phase-dependent flaring.

0.6. We show the individual TESS Sectors 42, 43, and 44 in panels A, B, and C, respectively. Panel D shows the combined data from all sectors, phase-folded on the orbital period and centered at the periastron time. As highlighted in Section 7.1, we do not see evidence for phase dependence of the flares.

Appendix B
Magnetic Field Structure Surrounding LHS 1610

Here, we show the alignment of the wind velocity and magnetic field vectors in the radial direction, and the fraction of open magnetic field lines, as a function of distance for the star Proxima Centauri (Figure 9) serving as an analog to LHS 1610. We use the stellar wind model presented in Kavanagh et al. (2021) for this. We see that the wind is predominantly oriented in the radial direction for distances greater than around 10 stellar radii, both in terms of the mass flow and magnetic field. This is necessary information for computing the angle θ between the vectors $\Delta \boldsymbol{u}$ and $\boldsymbol{B}_{\rm w}$, which in turn allows for the power dissipated via sub-Alfvénic interactions and auroral emission from the brown dwarf (Equations (26) and (32)).

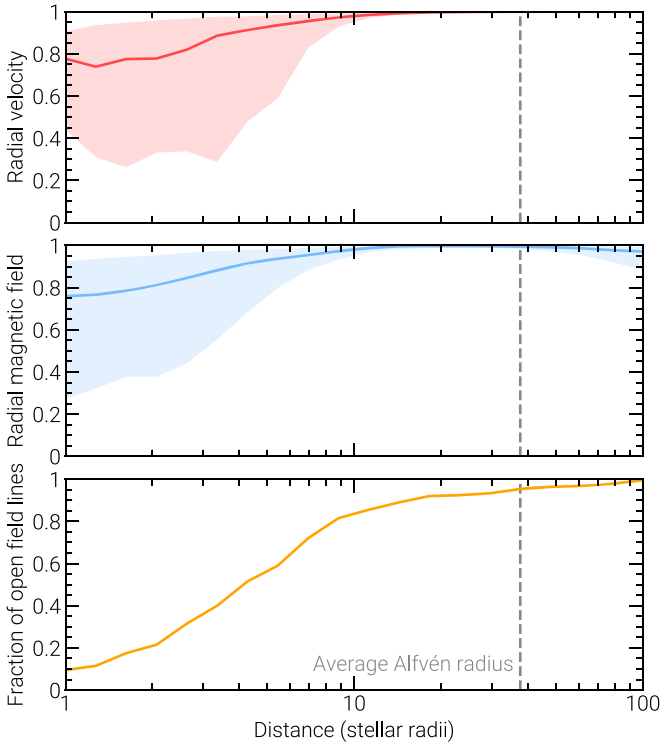

Figure 9. The fraction of the wind velocity (top) and magnetic field vectors (middle) that points in the radial direction, and the fraction of open field lines (bottom) as a function of distance for the wind of the LHS 1610 analog Proxima Centauri. The shaded regions in the top two panels show the 1σ interval, highlighting the variations in the wind inside the closed field. At distances greater than around 10 stellar radii, the wind flow direction and magnetic field becomes aligned with the radial direction. Note that this happens at a distance significantly smaller than the average size of the Alfvén radius, inside of which sub-Alfvénic interactions can occur between the star and companion, enhancing the activity of the star. Therefore, most sub-Alfvénic orbits experience a radial magnetic field.

Appendix C
Radial Velocities, Priors, and Joint-sampling Posteriors

Figure 10 shows the corner plot of the posterior distributions of the joint Gaia and RV sampling with the scaled Gaia covariance matrix ($\sigma_{\rm scale} > 1$) from Section 4.3. Table 4 lists the dates, radial velocities, and associated errors for the RVs from TRES and HPF. Table 5 lists the priors used in the RV-only, Gaia+RV without inflation, and Gaia+RV with inflation MCMC runs for reproducibility purposes.

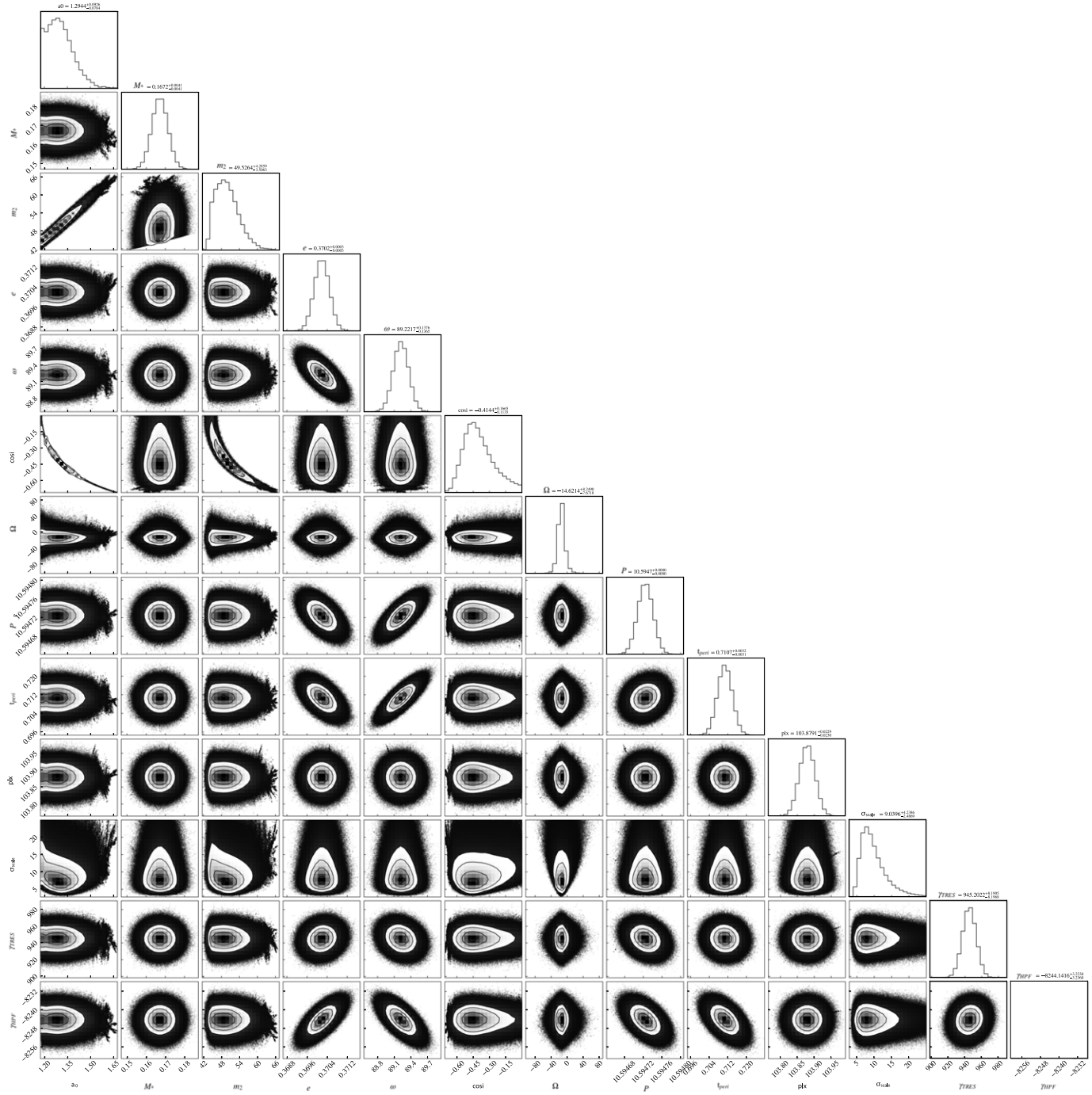

Figure 10. Corner plot showing the posterior distributions of the joint Gaia and RV sampling with the scaled Gaia covariance matrix ($\sigma_{\rm scale} > 1$) from Section 4.3. Median values are highlighted in Table 2.

Table 4
Radial Velocities for LHS 1610A

BJD (days)	RV (km s^{-1})	RV error (km s^{-1})	Instrument
2457785.7131	28.448	0.028	TRES
2457786.7850	32.365	0.028	TRES
2457787.6378	35.502	0.028	TRES
2457794.6483	22.514	0.028	TRES
2457795.7182	26.224	0.028	TRES
2457800.7416	44.533	0.028	TRES
2457806.6698	27.585	0.028	TRES
2457807.6875	31.293	0.029	TRES
2457808.6590	34.944	0.028	TRES
2457821.6194	43.586	0.028	TRES
2457822.6458	45.893	0.029	TRES
2457823.6552	40.479	0.031	TRES
2457824.6210	25.451	0.029	TRES
2459092.921787	−0.9804	0.0036	HPF
2459157.934541	1.1535	0.0028	HPF
2459185.659386	−10.612	0.003	HPF
2459212.786561	−21.375	0.006	HPF
2459274.599746	0.6958	0.0061	HPF
2459621.664956	−4.5927	0.0092	HPF

Note. TRES RVs are adopted as provided in Winters et al. (2018).

Table 5
Priors for the RV-only and Gaia+RV sampling

Parameter	RV-only Prior	Gaia+RV Prior—No Inflation	Gaia+RV Prior—Inflation
M_* ($M_\odot$)	…	$\mathcal{N}(0.1671, 0.0041)$	$\mathcal{N}(0.1671, 0.0041)$
m_2 ($M_{\rm Jup}$)	…	$\mathcal{U}(1.0, 100.0)$	$\mathcal{U}(1.0, 100.0)$
$\cos i$	…	$\mathcal{U}(-1.0, 0.0)$	$\mathcal{U}(-1.0, 0.0)$
i (deg)	…	…	…
K (m s^{-1})	$\mathcal{U}(100000., 200000.)$	…	…
e	$\mathcal{U}(0.0, 0.9)$	$\mathcal{U}(0.0, 0.9)$	$\mathcal{U}(0.0, 0.9)$
ω (deg)	$\mathcal{U}(0.0, 360.0)$	$\mathcal{U}(0.0, 360.0)$	$\mathcal{U}(0.0, 360.0)$
Ω (deg)	…	$\mathcal{U}(-180.0, 180.0)$	$\mathcal{U}(-180.0, 180.0)$
$t_{\rm peri}$ (days)[a]	$\mathcal{U}(-6.0, 6.0)$[a]	$\mathcal{U}(-6.0, 6.0)$[a]	$\mathcal{U}(-6.0, 6.0)$[a]
P (days)	$\mathcal{U}(10.5638, 10.6198)$[b]	$\mathcal{U}(10.5638, 10.6198)$[b]	$\mathcal{U}(10.5638, 10.6198)$[b]
ϖ (mas)	…	$\mathcal{N}(103.879, 0.023)$	$\mathcal{N}(103.879, 0.023)$
$\gamma_{\rm TRES}$ (m s^{-1})	$\mathcal{U}(-2000.0, 2000.0)$	$\mathcal{U}(-2000.0, 2000.0)$	$\mathcal{U}(-2000.0, 2000.0)$
$\gamma_{\rm HPF}$ (m s^{-1})	$\mathcal{U}(-17000.0, 17000.0)$	$\mathcal{U}(-17000.0, 17000.0)$	$\mathcal{U}(-17000.0, 17000.0)$
$\sigma_{\rm scale}$	…	1.0	$\mathcal{U}(1.0, 25.0)$
ε	…	0	0

Notes. Priors labeled $\mathcal{U}$ are uniform within those bounds. Those with $\mathcal{N}$ are normal priors, with the first value being the mean and the second value being the standard deviation of the Gaussian distribution. Priors with only a numerical value are fixed at that value.
[a] For the periastron time, we follow the Gaia convention where the periastron time is $t_{\rm peri} = 2457389.0 + t_p$, where t_p is the value listed in the table above.
[b] This prior is a $\pm 10\sigma$ window of the Winters et al. (2018) period of 10.5918 ± 0.0028 days. This encompasses the period from the Gaia two-body solution.

ORCID iDs

Evan Fitzmaurice https://orcid.org/0000-0003-0199-9699
Guðmundur Stefánsson https://orcid.org/0000-0001-7409-5688
Robert D. Kavanagh https://orcid.org/0000-0002-1486-7188
Suvrath Mahadevan https://orcid.org/0000-0001-9596-7983
Caleb I. Cañas https://orcid.org/0000-0003-4835-0619
Joshua N. Winn https://orcid.org/0000-0002-4265-047X
Paul Robertson https://orcid.org/0000-0003-0149-9678
Joe P. Ninan https://orcid.org/0000-0001-8720-5612
Simon Albrecht https://orcid.org/0000-0003-1762-8235
J. R. Callingham https://orcid.org/0000-0002-7167-1819
William D. Cochran https://orcid.org/0000-0001-9662-3496
Megan Delamer https://orcid.org/0000-0003-1439-2781
Eric B. Ford https://orcid.org/0000-0001-6545-639X
Shubham Kanodia https://orcid.org/0000-0001-8401-4300
Andrea S. J. Lin https://orcid.org/0000-0002-9082-6337
Marcus L. Marcussen https://orcid.org/0000-0003-2173-0689
Benjamin J. S. Pope https://orcid.org/0000-0003-2595-9114
Lawrence W. Ramsey https://orcid.org/0000-0002-4289-7958
Arpita Roy https://orcid.org/0000-0001-8127-5775
Harish Vedantham https://orcid.org/0000-0002-0872-181X
Jason T. Wright https://orcid.org/0000-0001-6160-5888

References

Akeson, R. L., Chen, X., Ciardi, D., et al. 2013, PASP, 125, 989
Anglada-Escudé, G., Amado, P. J., Barnes, J., et al. 2016, Natur, 536, 437

Astropy Collaboration, Robitaille, T. P., Tollerud, E. J., et al. 2013, A&A, 558, A33
Bailer-Jones, C. A. L., Rybizki, J., Fouesneau, M., Mantelet, G., & Andrae, R. 2018, AJ, 156, 58
Bellotti, S., Fares, R., Vidotto, A. A., et al. 2023, A&A, 676, A139
Blanco-Pozo, J., Perger, M., Damasso, M., et al. 2023, A&A, 671, A50
Bonomo, A. S., Desidera, S., Benatti, S., et al. 2017, A&A, 602, A107
Bowler, B. P., Blunt, S. C., & Nielsen, E. L. 2020, AJ, 159, 63
Brandt, G. M., Dupuy, T. J., Li, Y., et al. 2021, AJ, 162, 301
Buchhave, L. A., Bakos, G. Á, Hartman, J. D., et al. 2010, ApJ, 720, 1118
Burn, R., Schlecker, M., Mordasini, C., et al. 2021, A&A, 656, A72
Callingham, J. R., Vedantham, H. K., Shimwell, T. W., et al. 2021, NatAs, 5, 1233
Cañas, C. I., Mahadevan, S., Bender, C. F., et al. 2022, AJ, 163, 89
Chabrier, G., Johansen, A., Janson, M., & Rafikov, R. 2014, in Protostars and Planets VI, ed. H. Beuther, R. S. Klessen, C. P. Dullemond, & T. Henning (Tucson, AZ: Univ. Arizona Press), 619
Choi, J., Dotter, A., Conroy, C., et al. 2016, ApJ, 823, 102
Cohen, O. 2011, MNRAS, 417, 2592
Currie, T., Brandt, G. M., Brandt, T. D., et al. 2023, Sci, 380, 198
Damiani, C., & Díaz, R. F. 2016, A&A, 589, A55
Dotter, A. 2016, ApJS, 222, 8
Dulk, G. A. 1985, ARA&A, 23, 169
Dupuy, T. J., Liu, M. C., Best, W. M. J., et al. 2019, AJ, 158, 174
Duquennoy, A., & Mayor, M. 1991, A&A, 248, 485
Eastman, J. D., Rodriguez, J. E., Agol, E., et al. 2019, arXiv:1907.09480
Elekes, F., & Saur, J. 2023, A&A, 671, A133
Faria, J. P., Suárez Mascareño, A., Figueira, P., et al. 2022, A&A, 658, A115
Feinstein, A., Montet, B., & Ansdell, M. 2020a, JOSS, 5, 2347
Feinstein, A. D., Montet, B. T., Ansdell, M., et al. 2020b, AJ, 160, 219
Foreman-Mackey, D., 2016 corner.py: Scatterplot matrices in Python, v2.0.0, Zenodo, doi:10.5281/zenodo.53155
Foreman-Mackey, D., Hogg, D. W., Lang, D., & Goodman, J. 2013, PASP, 125, 306
Fulton, B. J., Petigura, E. A., Blunt, S., & Sinukoff, E. 2018, PASP, 130, 044504
Gaia Collaboration, Arenou, F., Babusiaux, C., et al. 2023, A&A, 674, A34
Gaia Collaboration, Prusti, T., de Bruijne, J. H. J., et al. 2016, A&A, 595, A1
Gaia Collaboration, Vallenari, A., Brown, A. G. A., et al. 2023, A&A, 674, A1
Gallet, F., Bolmont, E., Mathis, S., Charbonnel, C., & Amard, L. 2017, A&A, 604, A112
Gizis, J. E., Paudel, R. R., Mullan, D., et al. 2017, ApJ, 845, 33
Goldreich, P., & Soter, S. 1966, Icar, 5, 375
Gombosi, T. I., van der Holst, B., Manchester, W. B., & Sokolov, I. V. 2018, LRSP, 15, 4
Guillot, T., Burrows, A., Hubbard, W. B., Lunine, J. I., & Saumon, D. 1996, ApJL, 459, L35
Halbwachs, J. L., Mayor, M., & Udry, S. 2005, A&A, 431, 1129
Halbwachs, J.-L., Pourbaix, D., Arenou, F., et al. 2023, A&A, 674, A9
Henry, T. J., Jao, W.-C., Winters, J. G., et al. 2018, AJ, 155, 265
Hill, G. J., Lee, H., MacQueen, P. J., et al. 2021, AJ, 162, 298
Hogg, D. W., & Foreman-Mackey, D. 2018, ApJS, 236, 11
Holl, B., Fabricius, C., Portell, J., et al. 2023, A&A, 674, A25
Holl, B., Sozzetti, A., Sahlmann, J., et al. 2023, A&A, 674, A10
Howe, A. R., Mandell, A. M., & McElwain, M. W. 2023, ApJ, 951, L25
Hunter, J. D. 2007, CSE, 9, 90
Husser, T. O., Wende-von Berg, S., Dreizler, S., et al. 2013, A&A, 553, A6
Ilin, E., & Poppenhaeger, K. 2022, MNRAS, 513, 4579
Irwin, J. M., Berta-Thompson, Z. K., Charbonneau, D., et al. 2015, in 18th Cambridge Workshop on Cool Stars, Stellar Systems, and the Sun (Flagstaff, AZ: Lowell Observatory)
Jackson, B., Greenberg, R., & Barnes, R. 2008, ApJ, 678, 1396
Jardine, M., Vidotto, A. A., & See, V. 2017, MNRAS, 465, L25
Johnstone, C. P. 2017, A&A, 598, A24
Johnstone, C. P., & Güdel, M. 2015, A&A, 578, A129
Kanodia, S., & Wright, J. 2018, RNAAS, 2, 4
Kao, M. M., Hallinan, G., Pineda, J. S., Stevenson, D., & Burgasser, A. 2018, ApJS, 237, 25
Kavanagh, R. D., & Vedantham, H. K. 2023, MNRAS, 524, 6267
Kavanagh, R. D., & Vidotto, A. A. 2020, MNRAS, 493, 1492
Kavanagh, R. D., Vidotto, A. A., Klein, B., et al. 2021, MNRAS, 504, 1511
Kavanagh, R. D., Vidotto, A. A., Vedantham, H. K., et al. 2022, MNRAS, 514, 675
Klein, B., Donati, J.-F., Hébrard, É., et al. 2021, MNRAS, 500, 1844
Klein, B., Zicher, N., Kavanagh, R. D., et al. 2022, MNRAS, 512, 5067
Kluyver, T., Ragan-Kelley, B., Pérez, F., et al. 2016, in Positioning and Power in Academic Publishing: Players, Agents and Agendas, ed. F. Loizides & B. Scmidt (Amsterdam: IOS Press), 87
Lainey, V. 2016, CeMDA, 126, 145
Lainey, V., Arlot, J., Karatekin, O., & Van Hoolst, T. 2009, AAS, 41, 66.01
Lanza, A. F. 2018, A&A, 610, A81
Lattanzi, M. G., Spagna, A., Sozzetti, A., & Casertano, S. 2000, MNRAS, 317, 211
Lehmann, L. T., Donati, J. F., Fouqué, P., et al. 2024, MNRAS, 527, 4330
Li, Y., Brandt, T. D., Brandt, G. M., et al. 2023, MNRAS, 522, 5622
Lightkurve Collaboration, Cardoso, J. V. D. M., Hedges, C., et al., 2018 Lightkurve: Kepler and TESS time series analysis in Python, Astrophysics Source Code Library, ascl:1812.013
Ma, B., & Ge, J. 2014, MNRAS, 439, 2781
Magaudda, E., Stelzer, B., Covey, K. R., et al. 2020, A&A, 638, A20
Mahadevan, S., Ramsey, L., Bender, C., et al. 2012, Proc. SPIE, 8446, 84461S
Mahadevan, S., Ramsey, L. W., Terrien, R., et al. 2014, Proc. SPIE, 9147, 91471G
Mann, A. W., Dupuy, T., Kraus, A. L., et al. 2019, ApJ, 871, 63
Mann, A. W., Feiden, G. A., Gaidos, E., Boyajian, T., & von Braun, K. 2015, ApJ, 804, 64
Marcussen, M. L., & Albrecht, S. H. 2023, AJ, 165, 266
Marley, M. S., Saumon, D., Visscher, C., et al. 2021, ApJ, 920, 85
Mayor, M., Udry, S., Halbwachs, J. L., & Arenou, F. 2001, in IAU Symp. 200, The Formation of Binary Stars, ed. H. Zinnecker & R. Mathieu (Babelsberg: AIP), 45
Mazeh, T. 2008, in Tidal Effects in Stars, Planets and Disks (EAS Publications Series) Vol. 29ed. M. -J. Goupil & J. -P. Zahn (Les Ulis: EDP), 1
McKinney, W. 2010, in Proc. 9th Python in Science Conference, ed. S. van der Walt & J. Millman (Austin, TX: SciPy), 51
Medina, A. A., Winters, J. G., Irwin, J. M., & Charbonneau, D. 2020, ApJ, 905, 107
Medina, A. A., Winters, J. G., Irwin, J. M., & Charbonneau, D. 2022, ApJ, 935, 104
Meibom, S., & Mathieu, R. D. 2005, in ASP Conf. Ser. 333, Tidal Evolution and Oscillations in Binary Stars, ed. A. Claret, A. Giménez, & J. P. Zahn (San Francisco, CA: ASP), 95
Metcalf, A. J., Anderson, T., Bender, C. F., et al. 2019, Optica, 6, 233
Miguel, Y., Cridland, A., Ormel, C. W., Fortney, J. J., & Ida, S. 2020, MNRAS, 491, 1998
Narang, M., Manoj, P., & Ishwara Chandra, C. H. 2021, RNAAS, 5, 158
NASA Exoplanet Archive, Akeson, R.L., et al. 2013, PASP, 125, 989
Ninan, J. P., Bender, C. F., Mahadevan, S., et al. 2018, Proc. SPIE, 10709, 107092U
Nutzman, P., & Charbonneau, D. 2008, PASP, 120, 317
Parker, E. N. 1958, ApJ, 128, 664
Parviainen, H. 2016, PyDE, v1.5, Zenodo, doi:10.5281/zenodo.45602
Paudel, R. R., Gizis, J. E., Mullan, D. J., et al. 2020, MNRAS, 494, 5751
Pérez-Torres, M., Gómez, J. F., Ortiz, J. L., et al. 2021, A&A, 645, A77
Perryman, M., Hartman, J., Bakos, G. Á, & Lindegren, L. 2014, ApJ, 797, 14
Pineda, J. S., Hallinan, G., & Kao, M. M. 2017, ApJ, 846, 75
Pineda, J. S., & Villadsen, J. 2023, NatAs, 7, 569
Pont, F., Husnoo, N., Mazeh, T., & Fabrycky, D. 2011, MNRAS, 414, 1278
Pope, B. J. S., Callingham, J. R., Feinstein, A. D., et al. 2021, ApJL, 919, L10
Preusse, S., Kopp, A., Büchner, J., & Motschmann, U. 2005, A&A, 434, 1191
Raghavan, D., McAlister, H. A., Henry, T. J., et al. 2010, ApJS, 190, 1
Ramsey, L. W., Adams, M. T., Barnes, T. G., et al. 1998, Proc. SPIE, 3352, 34
Rasio, F. A., Tout, C. A., Lubow, S. H., & Livio, M. 1996, ApJ, 470, 1187
Reiners, A., & Christensen, U. R. 2010, A&A, 522, A13
Ricker, G. R. 2015, ESS, 47, 503.01
Rivera, E. J., Lissauer, J. J., Butler, R. P., et al. 2005, ApJ, 634, 625
Saur, J., Grambusch, T., Duling, S., Neubauer, F. M., & Simon, S. 2013, A&A, 552, A119
Saur, J., Willmes, C., Fischer, C., et al. 2021, A&A, 655, A75
Shetrone, M., Cornell, M. E., Fowler, J. R., et al. 2007, PASP, 119, 556
Shkolnik, E., Walker, G. A. H., Bohlender, D. A., Gu, P. G., & Kürster, M. 2005, ApJ, 622, 1075
Sozzetti, A., Casertano, S., Lattanzi, M. G., & Spagna, A. 2001, A&A, 373, L21
Sozzetti, A., Giacobbe, P., Lattanzi, M. G., et al. 2014, MNRAS, 437, 497
Stassun, K. G., Oelkers, R. J., Paegert, M., et al. 2019, AJ, 158, 138
Stassun, K. G., Oelkers, R. J., Pepper, J., et al. 2018, AJ, 156, 102
Stefansson, G., Hearty, F., Robertson, P., et al. 2016, ApJ, 833, 175
Stefansson, G., Mahadevan, S., Maney, M., et al. 2020, AJ, 160, 192
Stefánsson, G., Mahadevan, S., Miguel, Y., et al. 2023, Sci, 382, 1031

Stock, S., Kemmer, J., Reffert, S., et al. 2020, A&A, 636, A119
Tang, J., Tsai, C.-W., & Li, D. 2022, RAA, 22, 065013
Tannock, M. E., Metchev, S., Heinze, A., et al. 2021, AJ, 161, 224
Trigilio, C., Biswas, A., Leto, P., et al. 2023, arXiv:2305.00809
Turnpenney, S., Nichols, J. D., Wynn, G. A., & Burleigh, M. R. 2018, ApJ, 854, 72
Udry, S., Mayor, M., Delfosse, X., Forveille, T., & Perrier-Bellet, C. 2000, in IAU Symp. 200, Birth and Evolution of Binary Stars, ed. B. Reipurth & H. Zinnecker (Babelsberg: AIP), 158
Van Der Walt, S., Colbert, S. C., & Varoquaux, G. 2011, CSE, 13, 22
Vedantham, H. K., Callingham, J. R., Shimwell, T. W., et al. 2020, NatAs, 4, 577
Vidotto, A. A. 2021, LRSP, 18, 3
Vidotto, A. A., Fares, R., Jardine, M., et al. 2012, MNRAS, 423, 3285
Vieira, L. E. A., Kopp, G., Dudok de Wit, T., et al. 2022, ApJS, 260, 38
Villadsen, J., & Hallinan, G. 2019, ApJ, 871, 214
Weisskopf, M. C., Tananbaum, H. D., Van Speybroeck, L. P., & O'Dell, S. L. 2000, Proc. SPIE, 4012, 2
Winn, J. N. 2022, AJ, 164, 196
Winters, J. G., Irwin, J., Newton, E. R., et al. 2018, AJ, 155, 125
Wood, B. E., Müller, H.-R., Redfield, S., et al. 2021, ApJ, 915, 37
Wright, N. J., & Drake, J. J. 2016, Natur, 535, 526
Wright, N. J., Newton, E. R., Williams, P. K. G., Drake, J. J., & Yadav, R. K. 2018, MNRAS, 479, 2351
Yee, S. W., Petigura, E. A., & von Braun, K. 2017, ApJ, 836, 77
Zarka, P. 2007, P&SS, 55, 598
Zarka, P., Cecconi, B., & Kurth, W. S. 2004, JGRA, 109, A09S15
Zarka, P., Treumann, R. A., Ryabov, B. P., & Ryabov, V. B. 2001, Ap&SS, 277, 293
Zechmeister, M., Reiners, A., Amado, P. J., et al. 2018, A&A, 609, A12